Hydrodynamic simulations of mechanical stellar feedback in a molecular cloud formed by thermal instability

C. J. Wareing,[1][⋆] J. M. Pittard[1] and S. A. E. G. Falle[2]

[1]*School of Physics and Astronomy, University of Leeds, Leeds LS2 9JT, UK*
[2]*School of Mathematics, University of Leeds, Leeds LS2 9JT, UK*

ABSTRACT

We have used the AMR hydrodynamic code, MG, to perform 3D hydrodynamic simulations with self-gravity of stellar feedback in a spherical clumpy molecular cloud formed through the action of thermal instability. We simulate the interaction of the mechanical energy input from 15, 40, 60 and 120 $M_\odot$ stars into a 100 pc diameter 16 500 $M_\odot$ cloud with a roughly spherical morphology with randomly distributed high-density condensations. The stellar winds are introduced using appropriate non-rotating Geneva stellar evolution models. In the 15 $M_\odot$ star case, the wind has very little effect, spreading around a few neighbouring clumps before becoming overwhelmed by the cloud collapse. In contrast, in the 40, 60 and 120 $M_\odot$ star cases, the more powerful stellar winds create large cavities and carve channels through the cloud, breaking out into the surrounding tenuous medium during the wind phase and considerably altering the cloud structure. After 4.97, 3.97 and 3.01 Myr, respectively, the massive stars explode as supernovae (SNe). The wind-sculpted surroundings considerably affect the evolution of these SN events as they both escape the cloud along wind-carved channels and sweep up remaining clumps of cloud/wind material. The 'cloud' as a coherent structure does not survive the SN from any of these stars, but only in the 120 $M_\odot$ case is the cold molecular material completely destabilized and returned to the unstable thermal phase. In the 40 and 60 $M_\odot$ cases, coherent clumps of cold material are ejected from the cloud by the SN, potentially capable of further star formation.

Key words: hydrodynamics – stars: massive – stars: mass-loss – stars: winds, outflows – ISM: clouds – ISM: supernova remnants.

1 INTRODUCTION

The radiation fields, winds and supernovae (SNe) of massive stars destroy and disperse molecular material. This eventually ends star formation in clusters, though before that happens, massive stars may trigger further star formation (e.g. Koenig et al. 2012). The removal of mass from a cluster affects the cluster dynamics and plays a key role in cluster dissolution (Portegies Zwart, McMillan & Gieles 2010). Stellar feedback also sustains turbulence in the interstellar medium (ISM; e.g. Dobbs, Burkert & Pringle 2011) and powers galactic fountains and winds (Veilleux, Cecil & Bland-Hawthorn 2005). The mass, momentum, energy and ionizing radiation fluxes escaping a cluster into a galaxy, and beyond, depend on how stellar and SN energy output regulates cluster gas. However, the coupling of stellar winds, SNe and ionizing radiation to clumpy, inhomoge-

neous molecular clouds surrounding a massive stellar cluster is not well constrained.

Detections of diffuse X-ray emission from many young (pre-SN) massive star-forming regions support the conjecture that winds play important roles in clusters. Cold molecular material sometimes confines X-ray emitting gas, but around other clusters, hot gas appears to shape and remove cold clouds (e.g. Townsley et al. 2014). Direct evidence for large-scale outflows from stellar clusters is provided by observations of stellar bow shocks in and near clusters (e.g. Winston et al. 2012). 'Leakage' of the hot gas is also implied by the much lower mass of hot cluster gas than expected for the cluster ages and the mass-loss rates of stars (Townsley et al. 2003), and by energy budget considerations (Rosen et al. 2014). This leakage reduces the thermal pressure within the hot bubble enough that H II gas pressure may drive the dynamics (Harper-Clark & Murray 2009), at least for molecular clouds of $\sim 10^5$ $M_\odot$ (Dale, Ercolano & Bonnell 2012; Walch et al. 2012). Simulations of momentum-driven or isothermal winds (Dale, Ercolano & Bonnell 2015; Offner & Arce 2015) give a lower limit to their impact. Pre-SN

feedback enhances the impact of SNe (Fierlinger et al. 2016), and, in whole galaxy models, clears dense gas from star-forming regions, reducing the star formation rate (e.g. Agertz et al. 2013). However, whole galaxy models remain very sensitive to assumptions in the feedback scheme.

In our previous work (Rogers & Pittard 2013, 2014; Wareing et al. 2017), we have examined the effect that winds and SNe have on surrounding molecular material. In Wareing et al. (2017, hereafter Paper II), we explored the effect of mechanical feedback from a single 15 $M_\odot$ star and a single 40 $M_\odot$ star into a sheet-like molecular cloud formed by the action of the thermal instability under the influence of magnetic fields, which in projection appears remarkably filamentary. That cloud was one of three cases studied in Wareing et al. (2016, hereafter Paper I), which explored the formation of dense, cold, molecular clouds from quiescent diffuse thermally unstable clouds, under the influence of the thermal instability. There we considered the hydrodynamic case, the case of equal magnetic and thermal pressures and the case of dominating magnetic pressure (10 times greater than thermal pressure). Paper II explored feedback in the case of equal pressures. Here, we now explore the hydrodynamic case of feedback into a roughly spherical clumpy molecular cloud. We have presented a review of the relevant literature in Paper II and refer the interested reader back to that work.

In the next section, we present our numerical method and define the initial conditions used in our model, as well as the basis for realistic input of mechanical energy from each star. In Section 3, we present and discuss the resulting simulations, organized by results for the wind phase, the early SN phase and the late SN phase, rather than by each star. In Section 4, we present the global evolution with time of energy, density, phase, mass-weighted temperature–density and pressure–density distribution, total mass and mixing behaviour in each of our simulations. In Section 5, we compare our results to previous works and relevant observations. We summarize and conclude the work in Section 6.

2 NUMERICAL METHODS AND INITIAL CONDITIONS

2.1 Numerical methods

We present 3D, hydrodynamical (HD) simulations of stellar feedback with self-gravity using the established astrophysical code MG (Falle 1991) as recently used in Papers I and II. The code employs an upwind, conservative shock-capturing scheme and is able to employ multiple processors through parallelization with the message passing interface library. MG uses piece-wise linear cell interpolation to solve the Eulerian equations of hydrodynamics. The Riemann problem is solved at cell interfaces to obtain the conserved fluxes for the time update. Integration in time proceeds according to a second-order accurate Godunov method (Godunov 1959). A Kurganov–Tadmor Riemann solver is again used in this work (Kurganov & Tadmor 2000). Self-gravity is computed using a full-approximation multigrid to solve the Poisson equation. We reduce the Magneto-HD code to HD by setting all the magnetic field components to zero. For full details of the AMR method, please see Papers I and II. The simulations presented below employed eight levels of AMR. The physical size of the computational volume and the physical resolutions are as detailed below. Continued care has been taken with the implementation of realistic heating and cooling in the same way as used in Papers I and II.

2.2 Initial conditions

As well as creating filamentary molecular clouds through the effect of background magnetic fields and the influence of the thermal instability (Parker 1953; Field 1965), Paper I also explored the formation of clumpy molecular clouds in the zero-field case. In that work, we examined the evolution of diffuse clouds varying β, the ratio of thermal pressure to magnetic pressure. We examined three cases, $\beta = 0.1$, 1.0 and ∞, equivalent to the hydrodynamic case of zero magnetic field and of further interest here. In Paper I, the initial condition consisted of a stationary cloud of radius 50 pc with a number density of hydrogen throughout the cloud of $n_H = 1.1$ cm^{-3} giving the cloud a total mass of $\sim$16 500 $M_\odot$. In the cloud, 10 per cent density variations about the uniform initial density were introduced. The pressure was set according to the local density and thermal equilibrium between heating and cooling prescriptions at $P_{eq}/k = 4700 \pm 300$ K cm^{-3}, resulting in an initial temperature $T_{eq} = 4300 \pm 700$ K (an unstable part of the equilibrium curve – for more details see Paper I). An advecting scalar, α_{cloud}, was set equal to 1 in the cloud material. The pressure of the lower density ($n_H = 0.1$ cm^{-3}) surroundings was set equal to that of the unperturbed cloud, with α_{cloud} set equal to zero. No magnetic field was present in the simulation.

The computational volume consists of a 150 pc^3 box with free-flow boundary conditions (non-periodic for self-gravity) and AMR level G0 containing 4^3 cells. Eight levels of AMR mean an effective resolution of 512^3 cells on level G7, although by the time of the initial condition G2 with 16^3 cells is the finest fully populated level (rather than the MG default of G1). Extra tests have shown that we have resolved the action of the thermal instability. As previously noted in Papers I and II, such a large number of AMR levels are employed in order to efficiently compute the self-gravity on the coarsest levels and also fully resolve the structures formed in the molecular cloud. The finest physical resolution is 0.293 pc. The total number of cells across all eight AMR levels is 13.9 $\times$ 10^6 grid cells, 10 times less than that required by a fixed grid code with the equivalent 512^3 cells. The large number of AMR levels is computationally costly. Each 3D HD simulation with stellar feedback and self-gravity presented here with eight AMR levels took approximately 60 000 CPU hours ($\sim$10–12 48-h cycles on 128 cores of the high-performance computing facility at Leeds), so 240 000 CPU hours for the four runs presented. Supporting investigations included a parameter exploration of the initial condition (see Paper I) and a high-resolution rerun of the purely hydrodynamic case that also explored clump collapse to form pre-stellar cores. This costs more than the total CPU hours used by the simulations presented herein. Confidence in these simulations also comes from the results presented in Paper II. Each further level of AMR introduces a computational cost multiplier of between 6 and 8 for this model, given the spherical nature of the cloud, thus making complete higher resolution simulations prohibitively expensive at this time. Tests in Paper II showed that the resolution used is appropriate for these simulations, though it is close to the cooling length at times.

The influence of the thermal instability causes the cloud to evolve into multiple clumps. Specifically, molecular clumps form throughout the diffuse cloud. Self-gravity accelerates the contraction of the cloud. Besides exploring the importance of the thermal instability in molecular cloud evolution, the secondary aim of Paper I was to provide a more realistic initial condition for this work, by including more accurate heating and cooling, the effect of thermal instability, self-gravity and magnetic fields, as compared to our
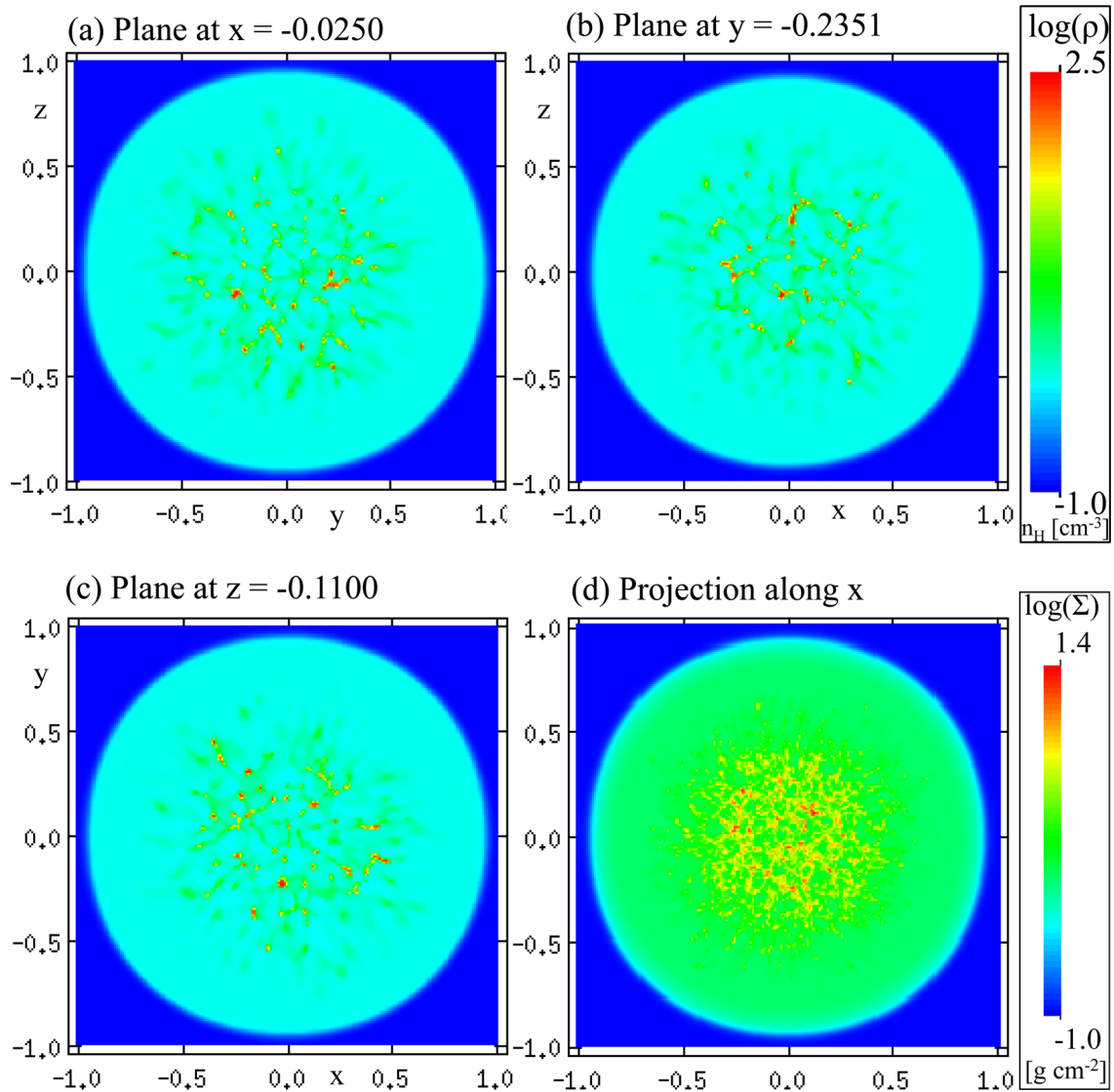
Figure 1. Initial condition. Snapshot of a clumpy cloud after 27.1 Myr of evolution used as the initial condition in this work. Shown are logarithm of mass density on planes (a) $x = -0.025$, (b) $y = -0.2351$, (c) $z = -0.11$ and projected column density along the x-axis in (d). Length is scaled in units of 50 pc. Raw data: doi.org/10.5518/201.

previous feedback studies (Rogers & Pittard 2013, 2014) where the clump structure was based upon the simulations of Vázquez-Semadini et al. (2008) of turbulent and clumpy molecular clouds and contained 3240 M$_\odot$ of material in a 4 pc radius.

In this work, we take as our initial condition a repeat of a cloud simulation without magnetic field following the method of Paper I. Different random seeds result in a simulation that is qualitatively the same as the result in Paper I, but quantitatively different. After 27.1 Myr of evolution, densities in the condensations formed in this new simulation have reached 100 cm^{-3} – the density threshold often used for injection of stars in similar simulation work (e.g. Fogerty et al. 2016). In this work, we have decided to inject stars at this time following the work of such other authors and also because of our own high-resolution simulations. We show snapshots of this initial condition in Fig. 1 and refer the interested reader to Paper I for a full description of the evolutionary process that led to the formation of this cloud. It is important to note though that this time-scale of 27.1 Myr should not be considered as the 'age' of the parent molecular cloud – this is the length of time required to go

from a diffuse cloud with an average density of $n_H = 1.1$ cm^{-3} to a structured molecular cloud where feedback can be introduced. Cold (less than 100 K) condensations in the cloud have only existed for a few Myr, in reasonable agreement with observed ages of molecular clouds.

In this paper, we consider four scenarios, each employing this initial condition, in order to examine the effect of stellar feedback in this cloud. We use the same method as Paper II, but repeat ourselves here for clarity in this work.

2.2.1 Scenario 1 – a 15 M$_\odot$ star

In this scenario, we introduce a 15 M$_\odot$ star at the position $(x, y, z) = (-0.025, -0.2351, -0.11)$ where the coordinates are given in scaled code units and the grid extends to $3 \times 3 \times 3$ centred on $(0, 0, 0)$. This is the location of the highest density condensation in the cloud, closest to the centre of the volume. We remove enough mass present in a spherical volume with a five-cell radius centred at this point to form a 15 M$_\odot$ star, assuming 100 per cent conversion of

cloud material to star. For this first investigation, the cloud mass in this spherical region is removed at the switch on of the stellar wind, $t_{wind} = 0$, under the assumption that this material has formed the star. If the mass is left in the injection region, the stellar wind rapidly and unrealistically cools and hence the feedback effects are significantly underestimated. An advected scalar, α_{wind}, previously set to zero throughout the grid, is set to 1 in the wind injection region in order to track the movement and mixing of the wind material.

For the stellar evolution, a 15 M$_\odot$ non-rotating Geneva stellar evolution model calculated by Ekström et al. (2012) is used in order to provide a realistic mass-loss rate over the lifetime of the star, as per the method used in Paper II. Detailed plots of this evolution can be found in Paper II. In this case, after 12 Myr of stellar evolution, the cloud has also collapsed under the influence of gravity. Densities in the centre of the cloud have reached levels where the resolution is insufficient so the simulation was stopped at this point, close to the end of the star's lifetime of 12.5 Myr. During the wind phase, the total mass and total energy injected by the star are 1.75 M$_\odot$ and 1.05×10^{49} erg, respectively. The location of the star remains constant throughout this simulation. The centre of cloud collapse is not exactly at the location of the star though, so in this case of a 15 M$_\odot$ star, a moving source is strictly required to accurately model this case. In future work, we plan to convert the mass into a 'star' particle following the method in MG of Van Loo, Butler & Tan (2013) and Van Loo, Tan & Falle (2015). The star can then move through the computational volume whilst feeding back through winds and SNe and remain consistent with self-gravity in the simulation.

2.2.2 Scenario 2 – a 40 M$_\odot$ star

In this scenario, we introduce a 40 M$_\odot$ star using the same method and at the same position as in Scenario 1, removing enough mass to form a 40 M$_\odot$ star from the spherical injection region. A 40 M$_\odot$ non-rotating stellar evolution model calculated by Ekström et al. (2012) is used in order to provide a realistic mass-loss rate over the lifetime of the star. Detailed plots of this evolution can be found in Paper II. The total mass and total energy injected by the star prior to SN explosion are 27.2 M$_\odot$ and 2.50×10^{50} erg, respectively. After 4.97 Myr, the star explodes as an SN, injecting 10 M$_\odot$ of stellar material and 10^{51} erg of energy into the same wind injection volume. The SN mass and energy is injected over 500 yr, roughly consistent with the time taken for a remnant to reach the size of the injection volume. An advected scalar, α_{SN}, previously set to zero throughout the grid, is set to 1 in the SN injection region in order to track the movement and mixing of the SN material. At this time, the wind scalar α_{wind} is set to zero. The fraction of cloud material in any given cell is $\alpha_{cloud} - \alpha_{wind} - \alpha_{SN}$.

Gravity plays less of a role during this shorter stellar wind phase as compared to the 15 M$_\odot$ star case and the early SN phase, partly due to the comparatively powerful dynamics and partly due to the shorter time-scale, but we continue to include it for consistency within the cloud and to explore the evolution post-SN when it again plays more of a role.

2.2.3 Scenario 3 – a 60 M$_\odot$ star

In this scenario, we introduce a 60 M$_\odot$ star using the same method and at the same position as in Scenario 1, removing enough mass to form a 60 M$_\odot$ star from the spherical injection region. A 60 M$_\odot$ non-rotating stellar evolution model calculated by Ekström et al. (2012) is used in order to provide a realistic mass-loss rate over the

lifetime of the star. The calculated mass-loss rate and wind velocity are shown in Fig. 2. Also shown in Fig. 2 are the energy injection rate and total injected mass. The total mass and total energy injected by the star prior to SN explosion are 47.5 M$_\odot$ and 8.9×10^{50} erg, respectively, almost equivalent to the energy introduced in the SN event and considerably more material. After 3.97 Myr, the star explodes as an SN in the same manner as in Scenario 2.

2.2.4 Scenario 4 – a 120 M$_\odot$ star

In this scenario, we introduce a 120 M$_\odot$ star using the same method and at the same position as in Scenario 1. In this case, we simply remove all the mass in a spherical region twice the size of the injection region in order to form the 120 M$_\odot$ star. A 120 M$_\odot$ non-rotating stellar evolution model calculated by Ekström et al. (2012) is used in order to provide a realistic mass-loss rate over the lifetime of the star. The calculated mass-loss rate and wind velocity are shown in Fig. 3. Also shown in Fig. 3 are the energy injection rate and total injected mass. The total mass and total energy injected by the star prior to SN explosion are 89.1 M$_\odot$ and 2.44×10^{51} erg, respectively, considerably more than the amount of material and energy introduced in an SN event. After 3.01 Myr, the star explodes as an SN in the same manner as in Scenario 2.

3 RESULTS

In this section, we present our results. We present both 2D slices through the computational volume created within MG and 3D contour and volume visualizations, created using the VISIT software (Childs et al. 2012). Raw data for all the figures in this paper are available from the University of Leeds Repository at doi.org/10.5518/201.

3.1 The wind phase

In Fig. 4, we show density slices through the computational volume during the evolution of the 15 M$_\odot$ star up to the end of its life. The low mass-loss rate and corresponding low-energy injection rate have minimal effect on the cloud structure, generating only a wind cavity that spreads away from the star into the cloud around the clumps for the first few Myr, but is eventually confined by the gravitational contraction of the cloud itself. All three planes through the location of the star reveal similar structure for all timepoints. This structure is a result of the weak wind that is able to affect the inter-clump material, but is not able to affect the high-density clumps themselves. Examining the extent of the stellar wind material, we see that very little wind material gets more than 10 pc away from the star.

During the red supergiant (RSG) phase of evolution, from $t_{wind}=11.2$ Myr until its SN explosion, the slow dense wind deposits considerable amounts of material into the cavity formed by the earlier wind and completely refills it. We do not show this stage of evolution here, as the cloud itself has collapsed and dominates the end stages of the stellar bubble's evolution. Neither do we trigger an SN in this simulation, as the cloud collapses to a high density that is unrealistic given our resolution.

In Fig. 5, we show the logarithm of density on all three planes through the location of the 40 M$_\odot$ star at various times through the star's lifespan. By only 0.707 Myr into the main-sequence evolution of the star, the impact on the molecular cloud is significant and clearly different from the 15 M$_\odot$ star case, as shown in the first row of Fig. 5. The stellar wind is expanding away from the star, streaming
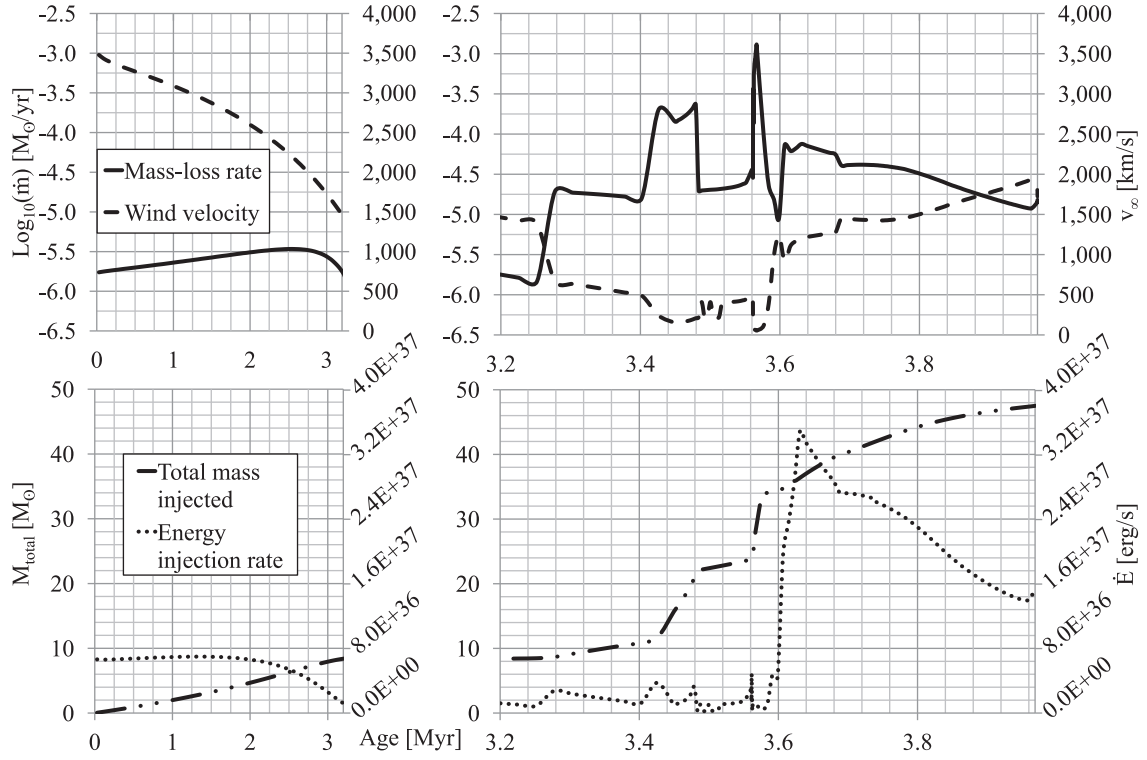
Figure 2. Stellar evolution tracks (Vink, de Koter & Lamers 2000, 2001; Ekström et al. 2012) for a 60 M$_\odot$ star, showing mass-loss rate and wind velocity on the upper graphs, and energy injection rate and total injected mass on the lower graphs. Raw data: doi.org/10.5518/201.
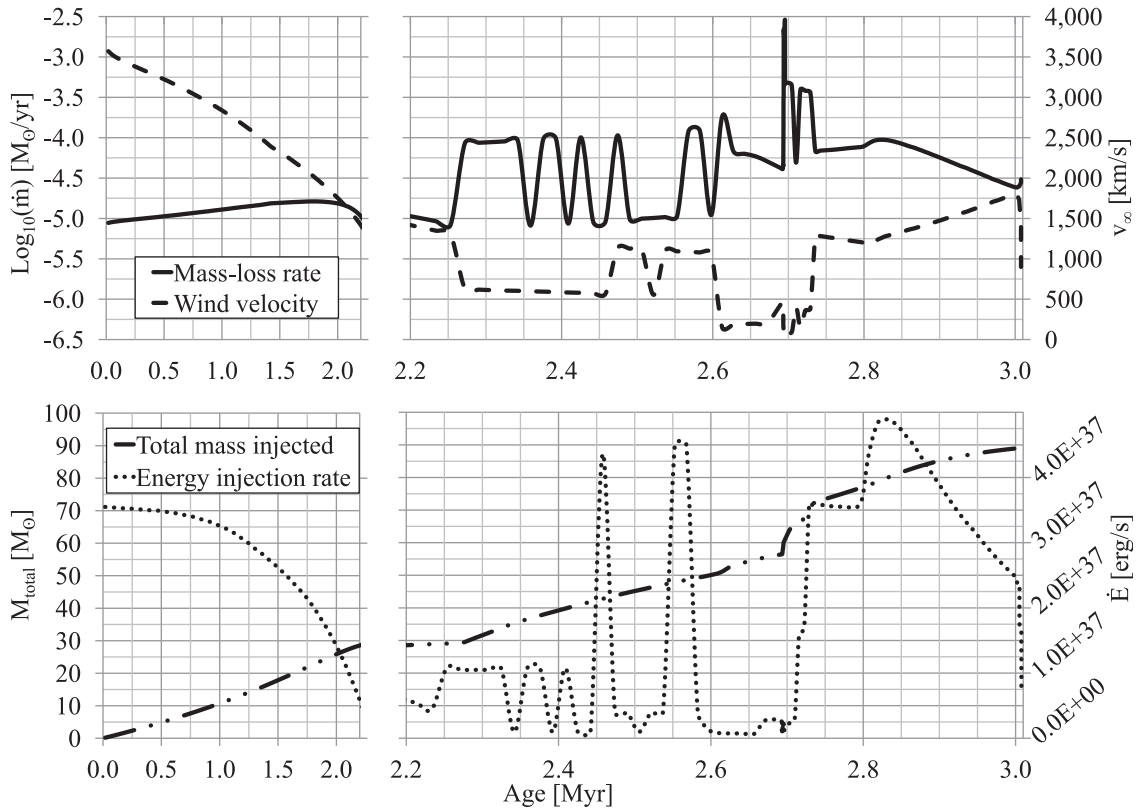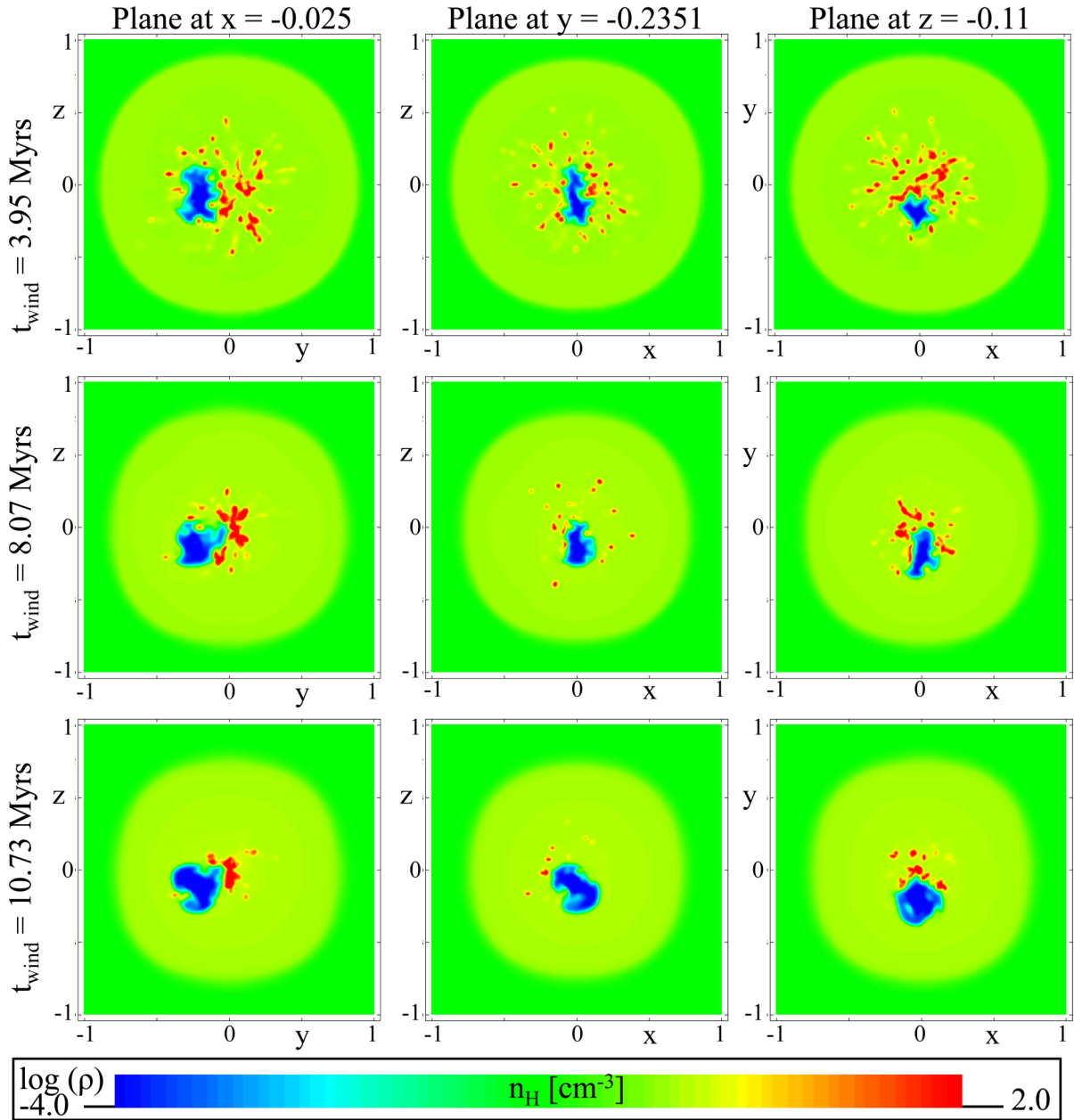

Figure 3. Stellar evolution tracks (Vink et al. 2000, 2001; Ekström et al. 2012) for a 120 M$_\odot$ star, showing mass-loss rate and wind velocity on the upper graphs, and energy injection rate and total injected mass on the lower graphs. Raw data: doi.org/10.5518/201.

Figure 4. Cloud–wind interaction during the lifetime of a 15 M$_\odot$ star. Shown is the logarithm of mass density at various times and on various planes through the computational volume. Length is scaled in units of 50 pc. Raw data: doi.org/10.5518/201.

past the clumps and already forming clear channels through the cloud. The wind is also beginning to ablate material from the clumps into the wind flow along the channels. By 1.53 Myr, as shown in the second row of Fig. 5, the wind has continued to expand, establishing a distinct reverse shock at a radius of approximately 5 pc. The ablated clumps are losing further material and being pushed away from the star – the force of the stellar wind on the clumps is clearly overcoming the gravitational contraction of the cloud and the wind is now blowing the cloud apart. After 3.01 Myr, the wind has reached the edge of the cloud material and can be seen in the *x*-plane expanding into the low-density surrounding medium. The wind has not yet escaped the cloud on the other planes, probably due to a combination of the centre-offset position of the star and the clump distribution in the cloud. A small number of low-density channels have now also become dominant in the structure, but by

4.42 Myr, at the end of the main-sequence evolution of the star, these channels have become less distinct on the *x*-plane, but more distinct on the *y*-plane. This structure, with its channels and clumps connected together, is reminiscent of our previous work (Rogers & Pittard 2013).

The star now enters the LBV phase. The wind mass-loss rate increases by two orders of magnitude to $\sim$10^{-4} M$_\odot$ yr^{-1}, and the terminal wind speed reduces to $\sim$100 km s^{-1}. This slow dense wind forms a high-density environment around the location of the star, which eventually contains $\sim$20 M$_\odot$ of LBV wind material. This phase lasts approximately 200 kyr and is followed by the WR phase of stellar evolution, where a variable, faster, less dense but more powerful wind sweeps up the LBV wind over the course of the final 400 kyr of the star's life. The structure formed is presented in the next section.
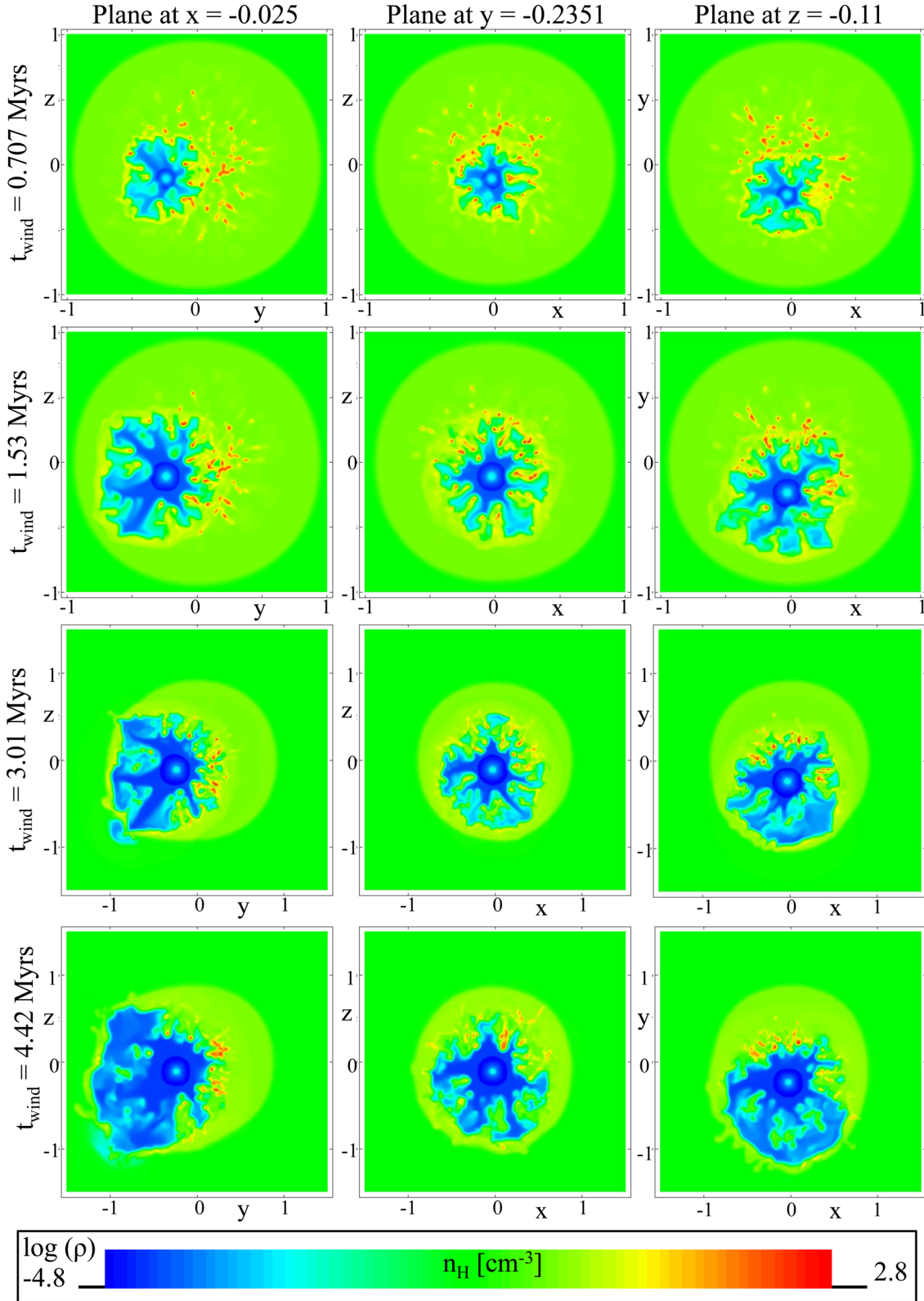
Figure 5. Cloud–wind interaction during the lifetime of a 40 M$_\odot$ star. Shown is the logarithm of mass density at various times and on various planes through the computational volume. Length is scaled in units of 50 pc. Raw data: doi.org/10.5518/201.

In Fig. 6, we show the logarithm of density on all three planes through the location of the 60 M$_\odot$ star at various times through the star's lifespan. After only 1.5 Myr, the impact on the molecular cloud is already almost equivalent to the total impact of the

40 M$_\odot$ star. The wind has carved channels to allow the flow of wind material out of the cloud and is now breaking out into the surrounding medium. After 3.3 Myr, at the end of the main-sequence evolution, the structure is more extreme, with several deep channels
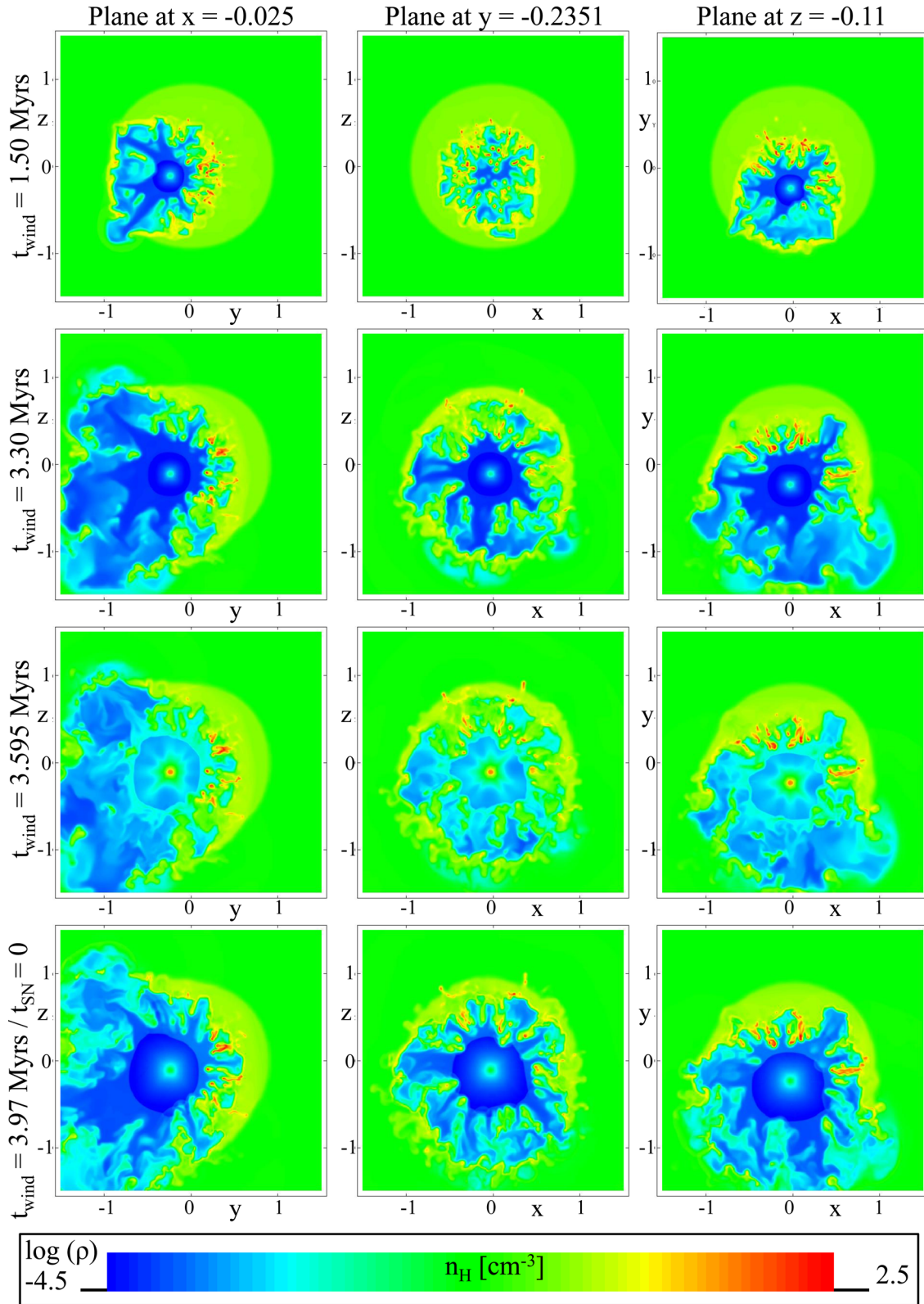
Figure 6. Cloud–wind interaction during the lifetime of a 60 M$_\odot$ star. Shown is the logarithm of mass density at various times and on various planes through the computational volume. Length is scaled in units of 50 pc. Raw data: doi.org/10.5518/201.

carved through the cloud and considerable amounts of wind material flowing out of the cloud. The reverse shock is clear and very close to spherical, almost isolated from the parent cloud, at a radius of approximately 20 pc from the star. Many clumps towards

the lower left of the star have been ablated and are mass loading the wind flowing away from the star. However, towards the upper left of the star, many of the clumps are still distinct, intact and still comparatively close to the star, especially compared to the now

close-to empty region towards the lower left of the *x*-plane. Clearly, the distribution of clumps and the position of the star play a key role in defining the wind-blown structure around the star.

After 2.74 Myr, the star enters the LBV phase and again the mass-loss rate increases and terminal wind speed reduces. As we saw also for the 40 M$_\odot$ scenario, this slow dense wind forms a high-density environment around the location of the star. We show the nature of the environment after this LBV phase along the third row of Fig. 6. After this, during the WR phase of stellar evolution, the variable, faster, less dense but more powerful wind is able to sweep the LBV and main-sequence material out into the cloud creating the final environment into which the SN will go off. By this time, the reverse shock is now up to 35 pc from the star and there are no traces of the high-density environment formed during the LBV phase. The large reverse shock structure dominates the cloud, outside which multiple channels will allow SN material to be transported rapidly out of the cloud. We note that some clumps have again survived this more extreme stellar evolution and remain relatively close to the star.

In Fig. 7, we show the logarithm of density on all three planes through the location of the 120 M$_\odot$ star at various times through the star's lifespan. The 120 M$_\odot$ star evolves through the main-sequence period in 2.24 Myr. The first two rows of Fig. 7 show the extreme effect this star has on its environment. By the end of the main sequence, half the cloud has been blown away, as shown in the *x*-plane. The reverse shock, previously relatively small, now approaches half the radius of the original cloud. It is almost spherical – the molecular cloud material has been carried out by the force of the stellar wind. In the *y*- and *z*-planes, channels through the cloud are clear. In the *z*-plane, some molecular cloud material is still reasonably close to the star, just outside the reverse shock. During the following LBV phase, multiple non-spherical shells form around the star, as shown in the third row of Fig. 7, caused by the oscillatory changes in the mass-loss rate and wind speed (see Fig. 3). The structure of the cloud is quite different depending upon which plane is considered. Low-density empty voids exist to the left in the *x*-plane and clumpy structure surrounds the shells formed during the LBV phase in the *y*-plane.

After the LBV phase, the variable, faster, less dense WR wind is able to evacuate the interior of the cloud in all directions, generating a strong reverse shock that in the empty void extends to more than 50 pc from the star. We show the final structure of the cloud at the end of the star's life, after 3.01 Myr, across the fourth row of Fig. 7. Much of the cloud has been swept away. Compared to the previous cases, the least amount of clumpy cloud material remains around the star – something we will study in more detail in the following analysis section.

In Fig. 8, we show column density, naive emission (calculated from the radiative cooling energy source term) and 3D visualizations of the cloud–wind structure at the end of the life of the three most massive stars. In the 40 M$_\odot$ star case, the blown-out side of the cloud is very clear in the column density plot. The radiative cooling plot highlights the 'emission' from the isolated LBV/WR shell very clearly, as discussed in more detail in the next sub-section. In the case of the 60 M$_\odot$ star, the column density projected along the *y*-axis highlights the fact that whilst the wind has blown out a larger section of the cloud than in the previous case (as shown in Fig. 6), the line of sight has strong effect on how obvious this blow-out is to the observer. The naive emission from the radiative cooling energy source term highlights the much greater extent of the more powerful WR wind in this case, reaching throughout the cloud. Column density shown collapsed along the *z*-direction for

the 120 M$_\odot$ star does show very clearly how much of the cloud has been dispersed from the original structure, as compared to how much is left in the top half of the cloud. Distinct in this plot and the plot for the 40 M$_\odot$ star are the radially aligned 'spokes' of the cloud after sculpting by the stellar wind. The hot, fast WR wind has triggered 'emission' all over the structure in the case of the 120 M$_\odot$ star. Of course, the 'emission' assumes optically thin conditions and true estimates of emission require radiative transfer to be simulated alongside the hydrodynamic evolution of the cloud–wind interaction. In the third column of Fig. 8, we show a complex 3D isosurface of the wind scalar on half the volume (indicated by the colour scale for the domain $x \leq 0$) and a second isosurface of the high-density clumpy cloud structure (indicated by the black isosurfaces at $\rho = 25$ cm^{-3}). In all three star cases, the yellow core highlights the inner core of the wind-blown bubble as well as the increasing extent of the wind-carved channels with greater stellar mass, reaching off the domain in many places for the case of the 120 M$_\odot$ star. Noticeable also from these 3D visualizations is the widening distribution of the high-density structure (indicated by the black clumps), dispersed by the increasingly powerful stellar winds with increasing stellar mass.

3.2 The early SN phase

The environment into which the SN mass and energy from the 40 M$_\odot$ star are injected is shown in Fig. 9(a). The non-spherical high-density shell structure formed during the WR stage of evolution is centred on the location of the star, distinct from, but strongly influenced by, the surrounding molecular cloud structure. In 4700 yr, the supernova remnant (SNR) has propagated far enough to fill the LBV/WR shell and after 7073 yr the SNR has overrun the shell and is now expanding into the star's wind-blown bubble, as shown in panels (b) and (c) of Fig. 9. After 10 000 yr, shown in panel (d), the forward shock of the SNR can clearly be seen expanding out into the bubble. Meanwhile, internal shocks reflecting off the inner shell are refilling the SNR. Clump remnants that had survived the wind phase are compressed by the SNR over the next 10 000 yr [panels (e) and (f)] and then accelerated outwards, towards the edge of the wind bubble. By 42 000 yr, in the final panel of Fig. 9, the internal shocks running back towards the location of the star from the edge of the wind bubble are acting to generate even more complex structure inside the SNR. The SNR now continues to expand, encompassing the wind bubble. The forward shock of the SNR reaches the edge of the grid after 69 000 yr, at the point where the SNR is closest to the edge of the grid in this panel.

In our previous work, studying the evolution of 40 M$_\odot$ star in a sheet-like cloud, we found that the stellar wind generated a tunnel through the cloud, through which the SNR was then able to escape the parent cloud in a matter of only 30 000 yr. Here, the SNR is able to progress through the wind-blown bubble equally as quickly, going beyond the extent of the original parent cloud where the wind-blown bubble had swept up and then beyond the molecular cloud itself. In other directions though, the SNR has been rapidly decelerated as it enters the parent molecular cloud – only in panel (e) of Fig. 9, 13 000 yr after the SN event, do we begin to clearly see the SNR progressing into clumpy cloud material. So in this case, as in the magnetically influenced case of the 40 M$_\odot$ star in Paper II, the wind-blown environment is the key to the evolution of the SNR. Progress in the hydrodynamic case is dramatically slowed by the denser clumps and the inter-clump material, as compared to progress through the low-density wind cavity. We now examine the same intra-cavity phase for the 60 and 120 M$_\odot$ stars.
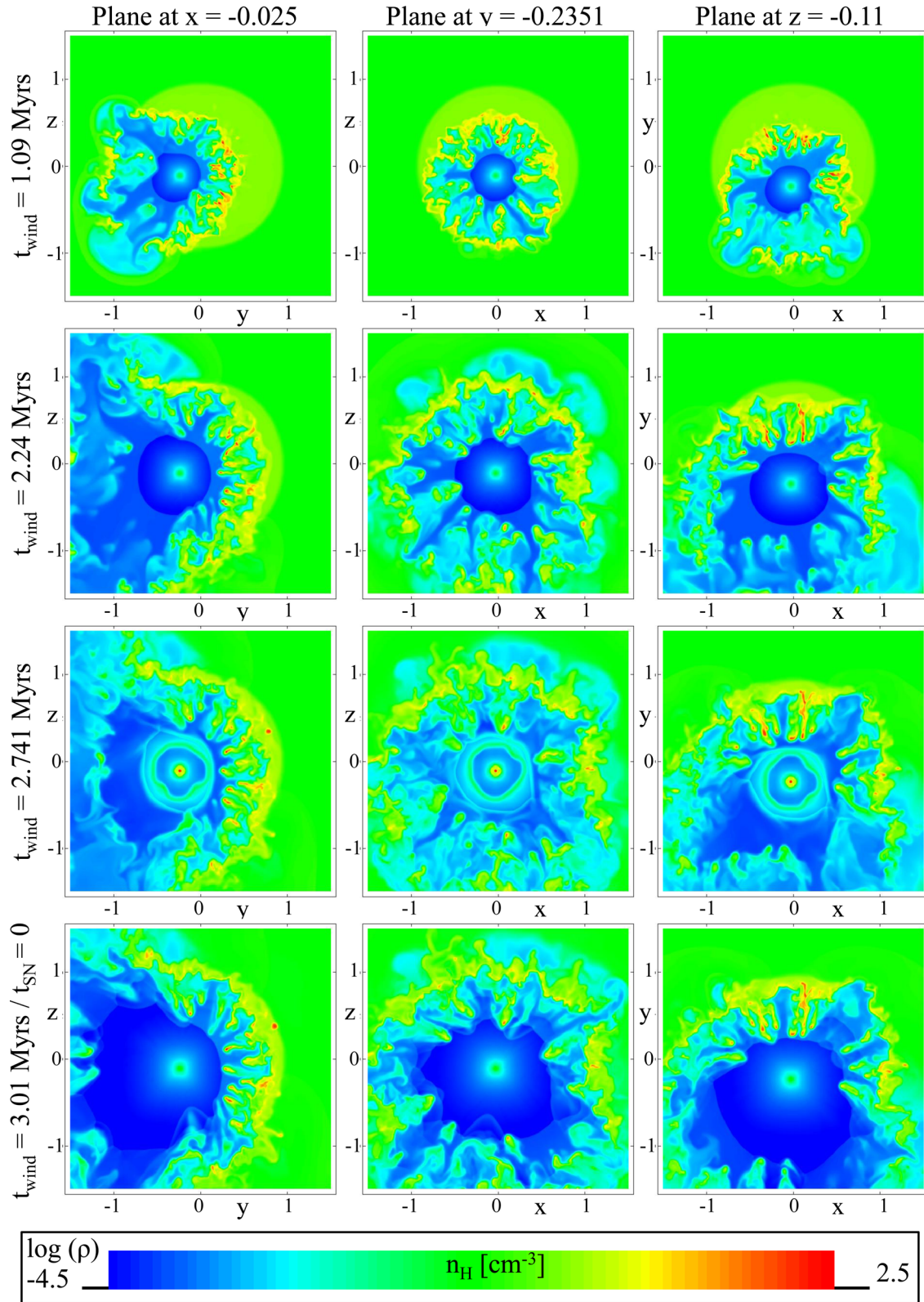
Figure 7. Cloud–wind interaction during the lifetime of a 120 M$_\odot$ star. Shown is the logarithm of mass density at various times and on various planes through the computational volume. Length is scaled in units of 50 pc. Raw data: doi.org/10.5518/201.

In Fig. 10, we show the logarithm of density on planes through the location of the 60 M$_\odot$ star at times after the SN event corresponding approximately to those shown in Fig. 9. Immediately clear in panel (a) is the larger size of the wind-blown bubble and

also the lack of any LBV/WR shell. The late-stage wind has blown out through the entire cavity formed in the preceding phase. The reverse shock of the WR wind is visible above and to the right of the star's location, located at a stand-off against the remaining clumpy
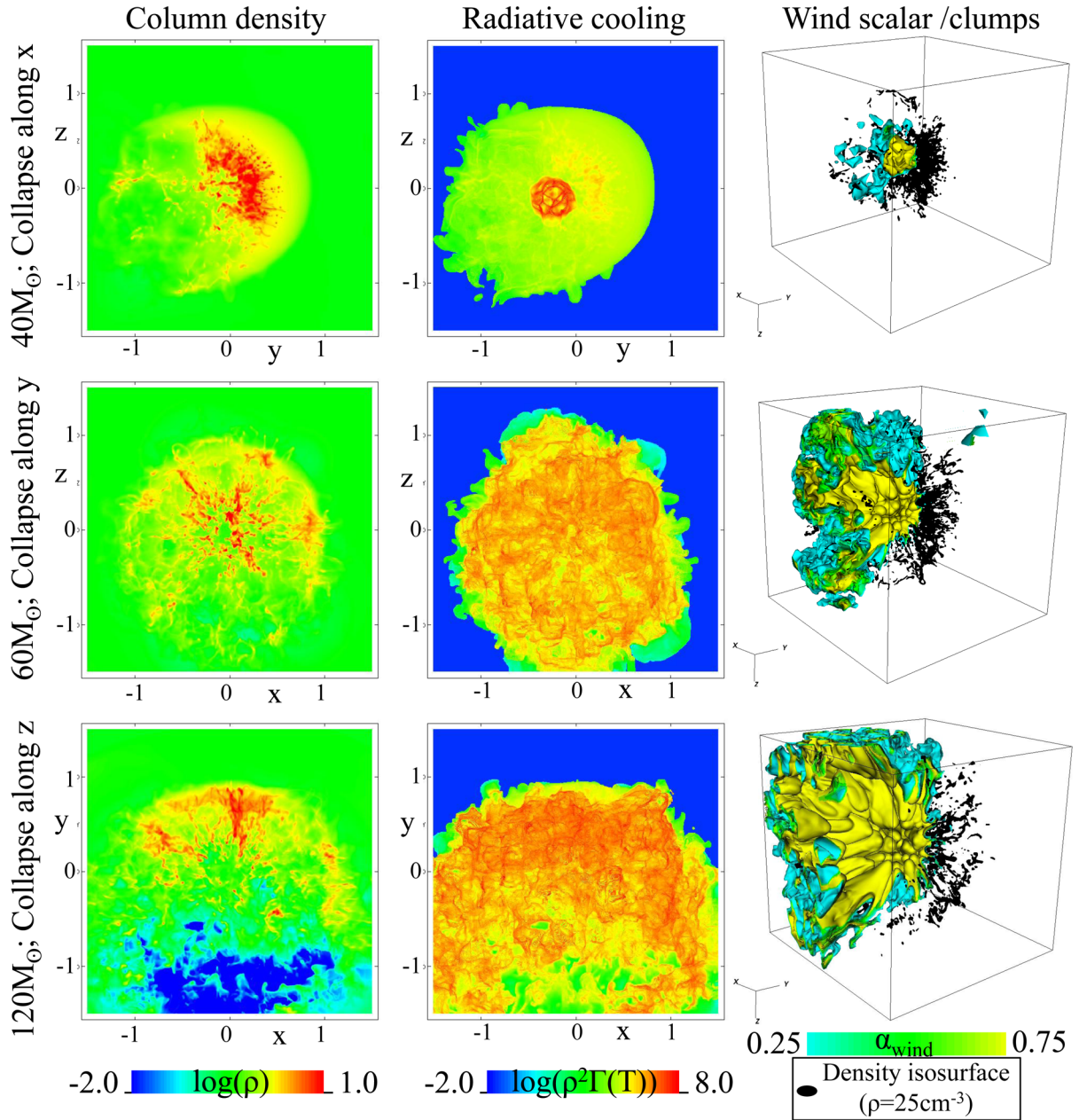
Figure 8. Column density, naive emission and 3D visualization of the cloud–wind structure just before each star goes SN. Naive emission is calculated as the radiative cooling energy source for each cell at this time, projected along the axes as defined in the figure. Length is scaled in units of 50 pc. Each 3D visualization shows the isosurface of the wind scalar (in colour) in half the computational volume ($x \leq 0$) in order to show the core of the wind-blown bubble and the distribution of high-density clumps (black isosurfaces) in the entire computational volume. Raw data: doi.org/10.5518/201.

cloud material. In the other directions, the shock of the WR wind is not visible in this figure due to the scaling chosen to show the SN evolution, but can be seen in the final row of Fig. 6. The SN explodes into this environment. For the first 4000 yr, the SNR expands into WR wind, unhindered by material from the preceding phases, or cloud material, as shown in panel (b). By 7000 yr, the SNR has passed the reverse shock of the WR wind in all directions and is now interacting with the remaining cloud material close to the star. Shocks are beginning to propagate down the channels between the network of clumps, whilst stand-off bow shocks are also forming ahead of the radial spokes of the network. Meanwhile, in the opposite direction, the SNR continues to expand into shocked LBV/WR wind material. This scenario of free expansion in one direction with

interaction in the other now describes the next 20 000 yr of SNR evolution as shown in the middle row of Fig. 10. Compared to the case of the 40 M$_\odot$ star, the wind structure is much larger and the channels off the grid have allowed the forward shock to leave the grid much earlier, specifically only 15 000 yr after the SN event, propagating down the widest wind-blown channel shown on the left of these panels. By 50 000 yr, the interactions of the SNR with this structure have set up multiple bow shocks that interact and form an even more complex structure. Channels allowing the early propagation of the SNR off the grid have now been filled with multiple wide bow-shock structures, as has the inside of the remnant. It is of particular interest here to note the survival of the spoke-like network of clumpy material to the left of the star. As the preceding wind
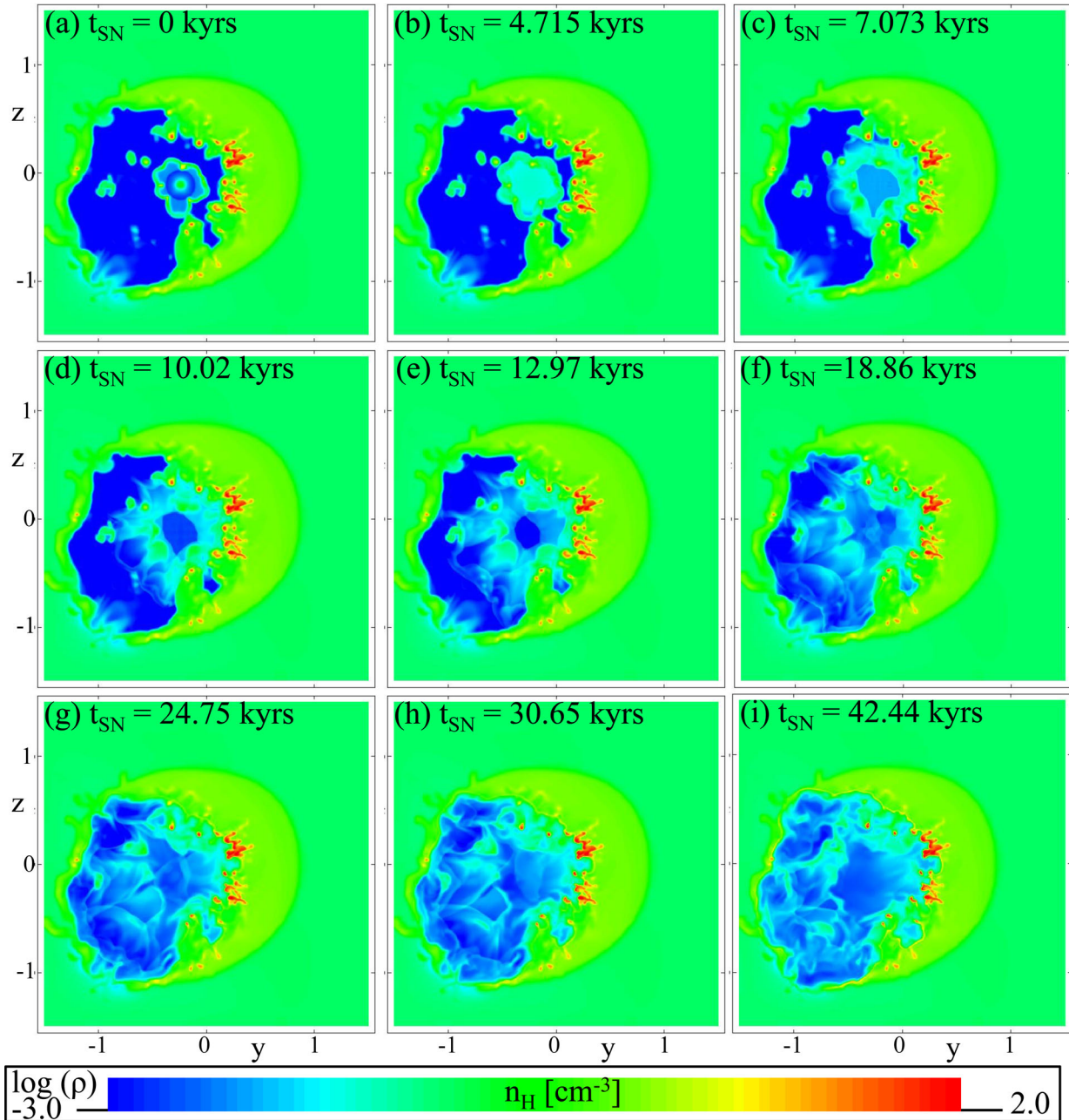
Figure 9. Early SN–cloud–wind interaction for a 40 M$_\odot$ star. Shown is the logarithm of mass density at various times on the plane at $x = -0.025$. Length is scaled in units of 50 pc. Raw data: doi.org/10.5518/201.

rearranged the individual clumps into aligned spokes, the cold cloud material aligned in the spokes is self-shielded against the passage of the SNR (and the preceding WR wind). Thus, whilst the head of each spoke is ablated, the length of the structures at 10–20 pc means much of the structure survives beyond this early stage of the SNR – clearly until at least 80 000 yr beyond the SN event, as shown in panel (i). We will explore the further evolution of these structures in the next sub-section and analyse the amount of cold cloud component remaining in the following section. Some slight numerical artefacts can be seen in the interior of the SNR at times, caused by derefinements of the AMR scheme in the smooth but ballistic and expanding flow. These have no effect on the passage of strong internal shocks, reflected off the cloud–wind structure, as can be seen across the third row of the figure.

In Fig. 11, we show the logarithm of density on planes through the location of the 120 M$_\odot$ star at times after the SN event corresponding approximately to those shown in Figs 10 and 11. Clear again in panel (a) is the greater effect upon the cloud of the stellar wind – half the cloud has been blown away. Again there is no LBV/WR shell – the reverse shock of the WR wind is visible to the right of the star's location, located at a greater stand-off distance against the remaining clumpy cloud material than in the case of the 60 M$_\odot$ star. In the other directions, the reverse shock of the WR wind is almost off the grid and far outside the original extent of the parent cloud ($r_{\rm cloud} \approx 1$). Panel (b) shows the SNR expanding into the undisturbed WR wind cavity for the first 5000 yr or so. After this time, the SNR passes the WR reverse shock boundary, creating internal structure at the edge of the SNR. It also begins to interact
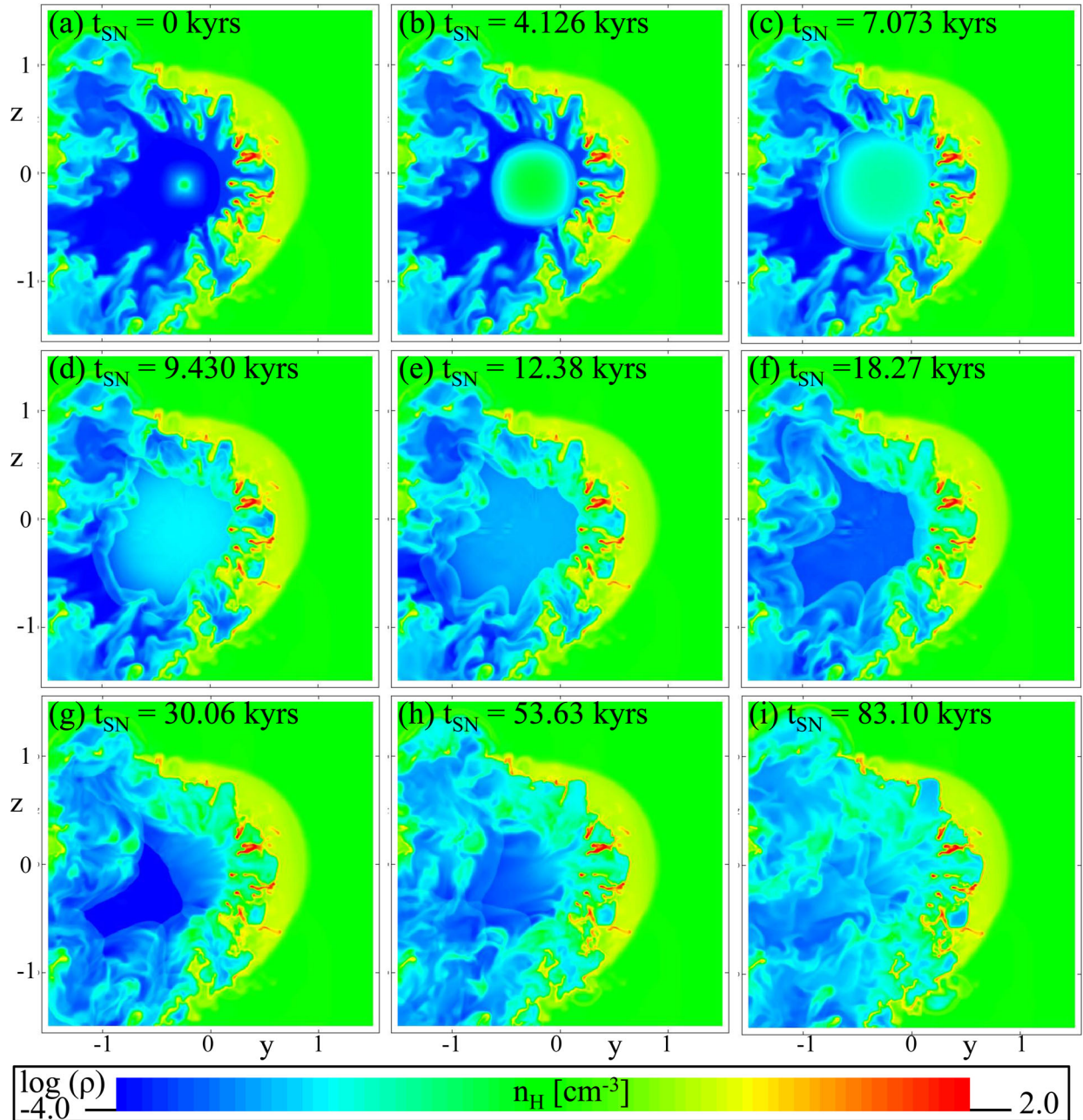
Figure 10. Early SN–cloud–wind interaction for a 60 M$_\odot$ star. Shown is the logarithm of mass density at various times on the plane at $x = -0.025$. Length is scaled in units of 50 pc. Raw data: doi.org/10.5518/201.

with the remaining 'spokes' of cold cloud material, ablating the inner end of the radially aligned spoke structure.

Over the next 10 000 yr (second row of Fig. 11), the forward shock of the SNR continues to expand into shocked WR wind material in one direction, whilst interacting with remaining cloud material in the other. This makes it easy to see how the SNR evolves differently under almost unhindered expansion versus expansion into multiple cold molecular clumps. This also highlights, as with the previous cases, that it is possible to observe *both* scenarios in one SN event. The forward shock leaves the grid after approximately 15 000 yr, similarly to the 60 M$_\odot$ star case. Across the third row of Fig. 11, it is possible to see the same SNR interaction behaviour as in the previous case of the 40 M$_\odot$ star, in that the SNR expands along the free channels, only in this case the left side of the cloud is

so dispersed that it is more like remnants of cloud material in a low-density shocked wind medium, than channels through shocked medium. For this reason, the bow shocks forming ahead of the remaining material against the SNR are not able to intersect to the extent that a reverse shock propagates back towards the explosion site. Indeed, the evolution of the bow shocks over time shows the relatively rapid cooling of these structures, as they fall back on to the clumps they were initially detached from. A large void in the centre of the SNR now exists. Evolving rapidly into this void, launched off the remaining cloud material to the right, is an internal shock. This can clearly be seen moving across the grid with a negative y-velocity in the bottom row of Fig. 11. By 50 000 yr, this structure has passed the original location of the SN event. This creates the observationally interesting scenario of an offset 'centre'
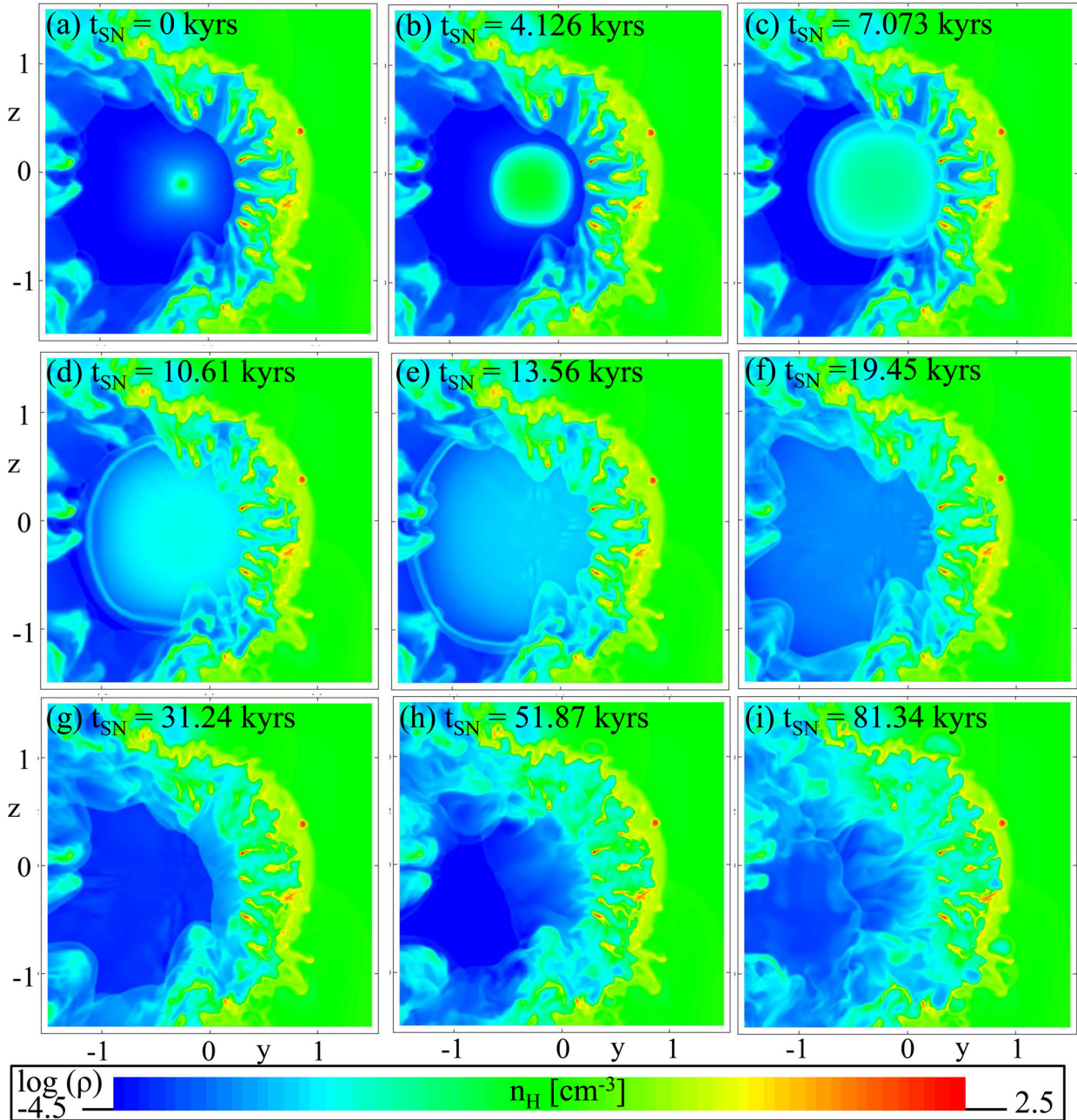
Figure 11. Early SN–cloud–wind interaction for a 120 M$_\odot$ star. Shown is the logarithm of mass density at various times on the plane at $x = -0.025$. Length is scaled in units of 50 pc. Raw data: doi.org/10.5518/201.

of the SNR, compared to the original location of the star (and the current location of any remaining stellar remnant). This particular simulation demonstrates the case of the stellar remnant being close to the edge of the SNR within a comparatively short 50 000 yr since the SN event.

3.3 The late SN phase

In Fig. 12, we show the late post-SN evolution of the 40 M$_\odot$ star simulation on y-planes through the location of the star. We show y-planes in this figure (as opposed to the x-planes shown for the early SN stage), as the SNR leaves the computational volume later on in the y-plane (due to the position of the star and structure of the cloud) and hence boundary effects come into play later on this plane. After

98 000 yr, as shown in panel (a), the SNR can be seen escaping the molecular cloud, having now swept up the wind material into the thin shell, punctured by the spokes of remaining cloud material. Over the next few hundred thousand years, internal shocks bounce back from the edge of the SNR, and the ablation of the remaining cloud material increases due to the passage of these shocks within the internal void of the SNR. The SNR has also expanded and cooled far enough to reach the radiative phase of evolution. In panel (b), the forward shock is becoming subject to Rayleigh–Taylor instabilities and beginning to break up into individual clumps, in the same way as noted previously in Paper II. The remnants of the molecular cloud survive this phase reasonably well.

By 1.51 Myr, the forward shock of the SNR has reached the edge of the computational volume and the simulation after this
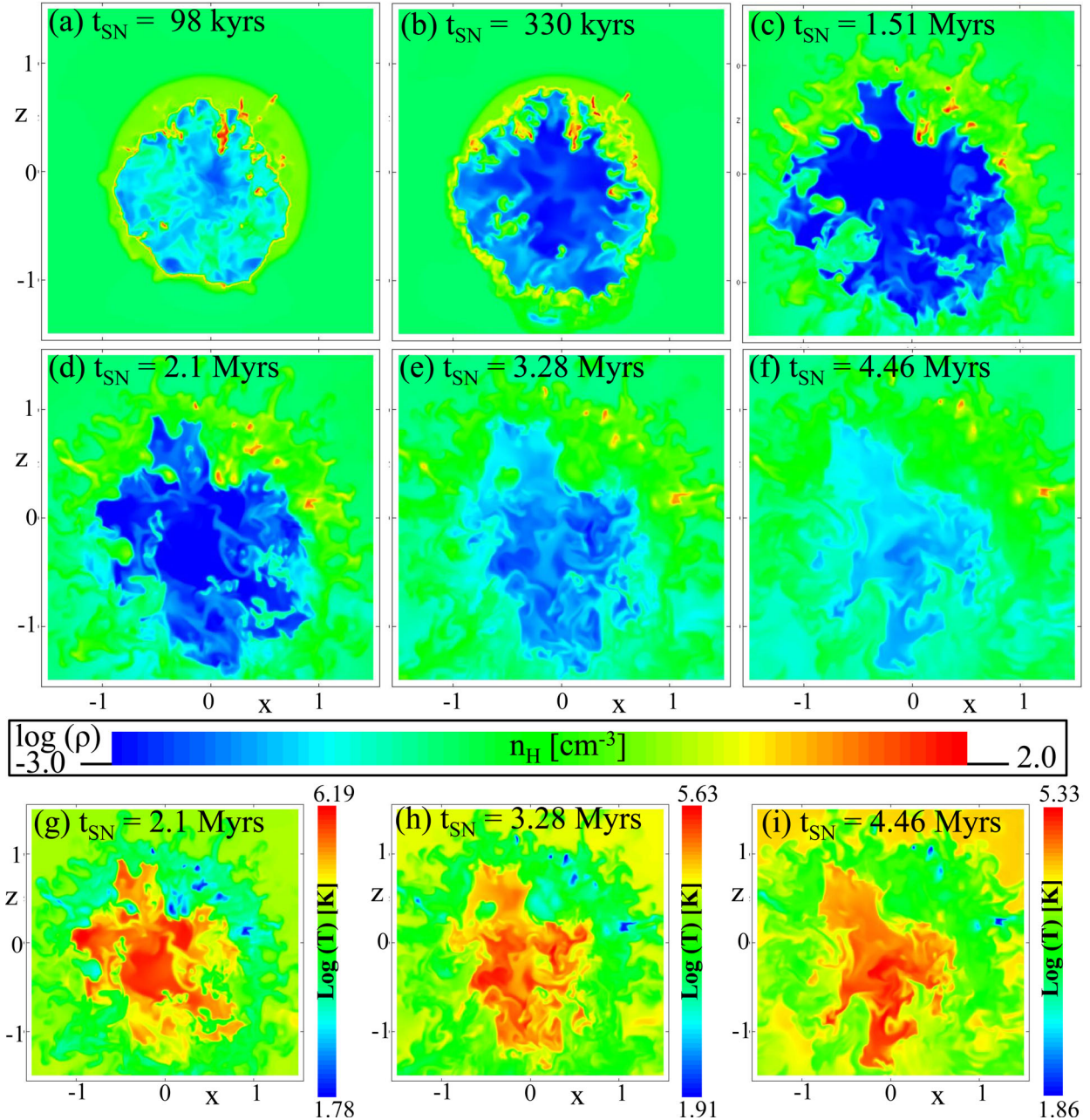
Figure 12. Late SN–cloud–wind interaction for a 40 M$_\odot$ star. Shown is the logarithm of mass density and temperature at various times on the plane at $y = -0.2351$. Length is scaled in units of 50 pc. Raw data: doi.org/10.5518/201.

point should not be taken too literally, since boundary effects have come into play. Nevertheless, the later evolution can be used as a guide to the sort of behaviour one might expect to see. We are now particularly interested in the fate of the remaining cloud material. Considering the second row of panels, (d) at 2.1 Myr, (e) at 3.28 Myr and (f) at 4.46 Myr post-SN, it is clear that the molecular cloud has been dispersed as all that is left are a few disparate high-density clumps. It is clear by looking at the temperature plots at equivalent times, as shown in the third row of the figure, that these are still cold (≤ 100 K), even after the passage of the SNR and are the final remaining parts of the molecular cloud. The structure of the cloud is destroyed, but parts of the cold cloud material remain, much as occurred in the case of the 40 M$_\odot$ star in a magnetically collimated sheet-like cloud in Paper II. As also noted in Paper II, self-gravity

in the dispersed clumps is now likely to dominate their evolution, possibly leading to further star formation. It is highly likely that the disruption of the molecular cloud is caused by the SN event and not influenced by any numerical effects, as the outward motion of the clumps can be traced back to before the SNR reached the edge of the computational volume. We will consider in the following cases whether this can be confirmed further, by examining the rate of cloud destruction in each case, but to be more confident of this result, future computationally costly simulations with a larger volume are necessary. Further questions over the fate of the remaining molecular material and whether the SN triggers any further formation of cold material by disrupting the thermal stability of the wind/cloud material are addressed in Section 4. Some indications are given by the decreasing lower limit of the temperature range
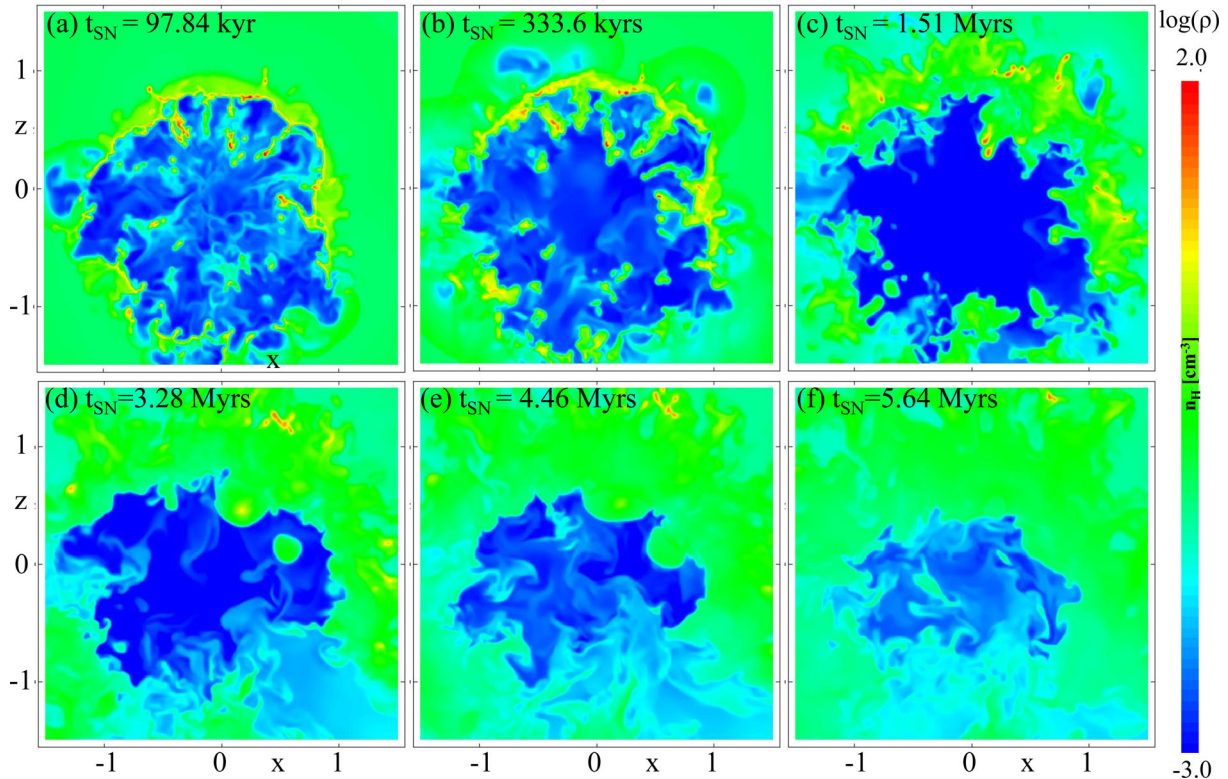
Figure 13. Late SN–cloud–wind interaction for a 60 M$_\odot$ star. Shown is the logarithm of mass density at various times on the plane at $y = -0.2351$. Length is scaled in units of 50 pc. Raw data: doi.org/10.5518/201.

going from panels (h) to (i), indicating the presence of ever-colder material on this plane. Note also the 'turbulent' nature of the interior of the SNR, caused by the interaction of multiple shocks. Even after 2 Myr, the temperature inside the SNR is still above 10^6 K. The SNR cools noticeably over the next 2.5 Myr. With a cooling and dispersing remnant, gravity plays an increasingly important role. We have simulated on to 6 Myr post-SN, but are unable to confidently assess the balance in the simulation between the evolution caused by the SNR, by gravity and by the influence of any boundary effects.

In Fig. 13, we show the late post-SN evolution of the 60 M$_\odot$ star simulation. Whilst structural similarities to the 40 M$_\odot$ case are apparent, it should be noted that the SNR is larger and has left the cloud at a much earlier time. Clearly, the major reason is the enhanced disruption of the cloud by the wind during the preceding evolution. While the SNR transitions into the radiative phase at around the same time, comparing panel (b) in both this and Fig. 12, it is clear that the rest of the remnant is much more dispersed. The same effects come into play as the star evolves into Myr post-SN, but in this case it should be noted that the clumpy remains of the molecular cloud are fewer and further out from the star. We show the SNR at 5.64 Myr post-SN to display the final turbulent state of the SNR. We analyse the evolution of the cold molecular material in the computational volume as a whole in the next section.

In Fig. 14, we show the late post-SN evolution of the 120 M$_\odot$ star simulation. The effect of the preceding wind phase – to allow the SNR to have completely blown through the wind-cloud structure in the *y*-plane after only 100 000 yr – is shown in panel (a). A slight 'echo' of the edge of the cloud remains, but otherwise turbulent conditions dominate the interior of the SNR. This arc-like echo of the cloud breaks up after 300 000 yr of SNR evolution. After 1.5 Myr, the last few high-density cloud components are leaving the

grid. After this, a low-density SNR void is surrounded by average ISM conditions (densities ranging from 10^{-2} to 10^0 particles per cm^3). There are no cloud components left on this plane – the cloud has been completely dispersed by the SNR.

4 ANALYSIS

4.1 Energy

In Fig. 15, we show how the distribution of energy between kinetic, thermal and hot thermal (i.e. material above 10 000 K) in the cloud, wind and SN material combined varies over time following the introduction of stellar feedback, with reference to a simulation of the cloud evolution without feedback for each star. The thermal and kinetic energy fractions together sum to 1.0, i.e. we are ignoring gravitational energy in this figure. Note that the hot thermal profile indicates the fraction of the thermal energy that is 'hot'. In the second plot for each star, we show how the total energy in the cloud varies over time, with reference to the simulations of the cloud without feedback. The third plot for the 40, 60 and 120 M$_\odot$ star cases shows the post-SN 'radiated and escaped energy', i.e. energy that is radiated away or leaves the grid dynamically – we do not differentiate between these two means of energy loss in the plot.

For the first 10 Myr of the 15 M$_\odot$ star case, the energy fractions do not change considerably during the wind phase, as compared to the reference case. This was expected from the minimal dynamic and structural impact the star has on the cloud. In fact, the stellar wind introduces so little energy that the overall energy in the cloud reduces over the first 10 Myr of the star's life, as compared to the 'no feedback' reference case. This likely arises due to relatively efficient radiative cooling of the predominantly thermal energy
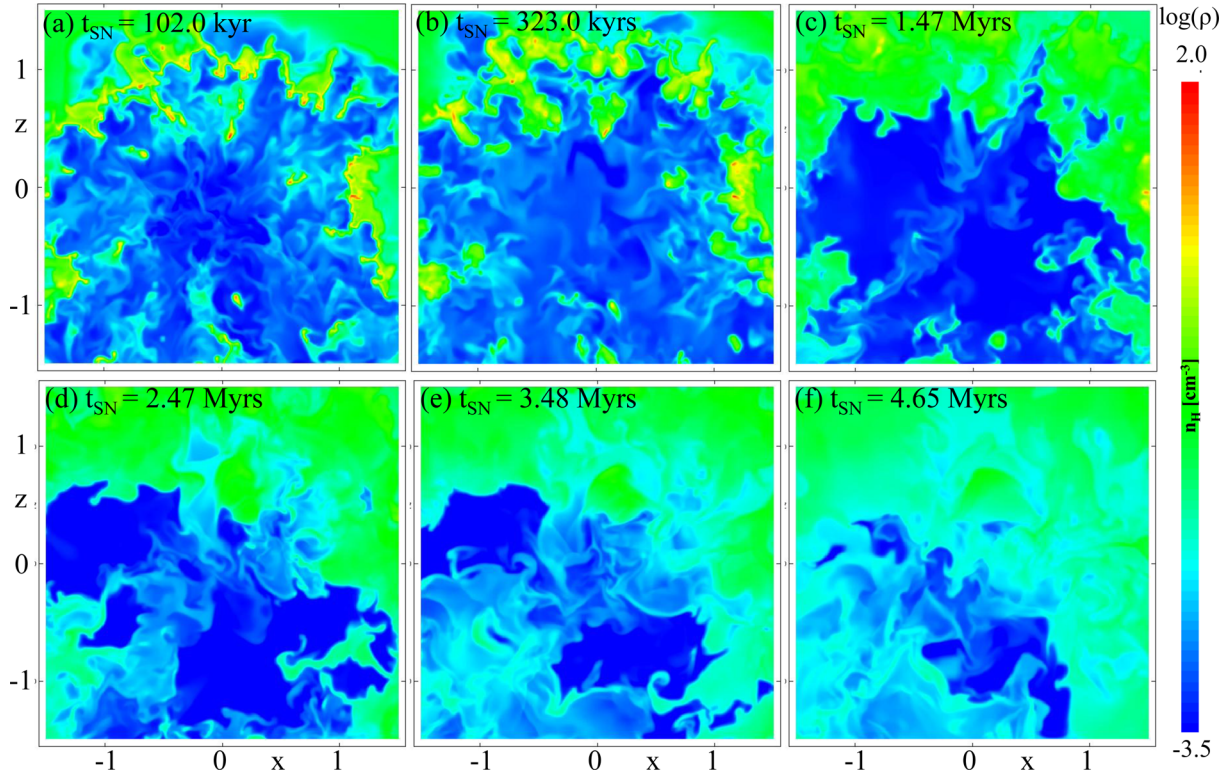
Figure 14. Late SN–cloud–wind interaction for a 120 M$_\odot$ star. Shown is the logarithm of mass density at various times on the plane at $y = -0.2351$. Length is scaled in units of 50 pc. Raw data: doi.org/10.5518/201.

injected by the stellar wind, perhaps due to weakly compressing and heating neighbouring cloud material. From 10 Myr post-star formation (37 Myr in the figure), the collapse of the cloud dominates the evolution. The stellar wind has little effect on this and after 37 Myr, these results contain no meaningful information.

In the 40 M$_\odot$ star case, the stellar wind has a clear effect on the energy fractions during the wind phase. The stellar wind supplies and creates large amounts of kinetic and hot thermal energy, raising both fractions above the close-to-zero reference case. Given that the wind blows a hot bubble, it is likely that radiative losses are responsible for the drop in total energy approaching the end of the star's life, before the introduction of 10^{51} erg of thermal energy and 10 M$_\odot$ of material in the SN event. The introduction of this thermalized SN kinetic energy is most obvious in the total energy plot, as the spike just after 32 Myr. Since the SN energy is injected thermally, both the thermal energy and the 'hot thermal' phase rise sharply at this time. The third plot for the 40 M$_\odot$ star case shows that the SN energy is rapidly transported and radiated out of the simulation. Note that the forward shock of the SNR first reaches the edge of the computational volume approximately 69 000 yr after the SN event. At approximately 1 Myr post-SN, the energy balances are most different from the reference case without feedback (apart from the first few thousand years of SN evolution, which we discuss in more detail later in this sub-section). After this, as the SNR escapes from the cloud/wind structure into the surroundings and then off the grid, the kinetic energy fraction falls and the thermal energy fraction rises. This behaviour continues, albeit at a decreasing rate, until the end of the simulation. The actual amount of thermal energy drops until approximately 2.5 Myr post-SN and then plateaus, whereas the kinetic energy simply continues to drop during the simulation post-SN. The plateauing of thermal energy

corresponds to when the hot thermal fraction of energy remaining on the grid has fallen to close to zero – much of the material on the grid has now dropped to temperatures below 10 000 K and densities in the range 0.01–1 cm^{-3}, with random motions at a range of velocities and scales (except for the last remaining gas in the hot, central void of the SNR, but this is at low density). This is fairly characteristic of the warm, neutral medium, formed in this case from evolution of an isolated single star, approximately 2.5 Myr post-SN.

In the 60 M$_\odot$ star case, the wind effect upon the thermal and kinetic energy fraction is an amplified version of the 40 M$_\odot$ star case. During the main-sequence wind phase, the amounts of both thermal and kinetic energy on the grid increase smoothly for 2.5 Myr, then decrease smoothly, with the amount of kinetic energy increasing and decreasing more than thermal energy. In the final stages of the star's evolution, the total energy in the simulation is increased by a factor of 5 by the stellar wind, with a sharp increase in amounts of both thermal and kinetic energy. This corresponds closely with the increased energy injection rate of the stellar wind, as shown in Fig. 2. The kinetic energy increases by a factor of 10, leading to the apparent drop in the thermal energy fraction, although there is no drop in the actual amount of energy. Just before the SN, 10 times more energy is present in the simulation than in the reference case, or the 40 M$_\odot$ star case (which is close to the reference case pre-SN). One must bear in mind that a substantial amount of the total wind energy up to this point has already been transported off the grid, while some has also been radiated away.

The SN event increases the amount of energy on the grid by a factor of 10. The post-SN evolution of the energy fraction and the total energy in the simulation evolves in a similar way to the 40 M$_\odot$ star case, with an initial peak in kinetic energy (and trough in thermal energy) as the SNR blows out of the cloud. In this
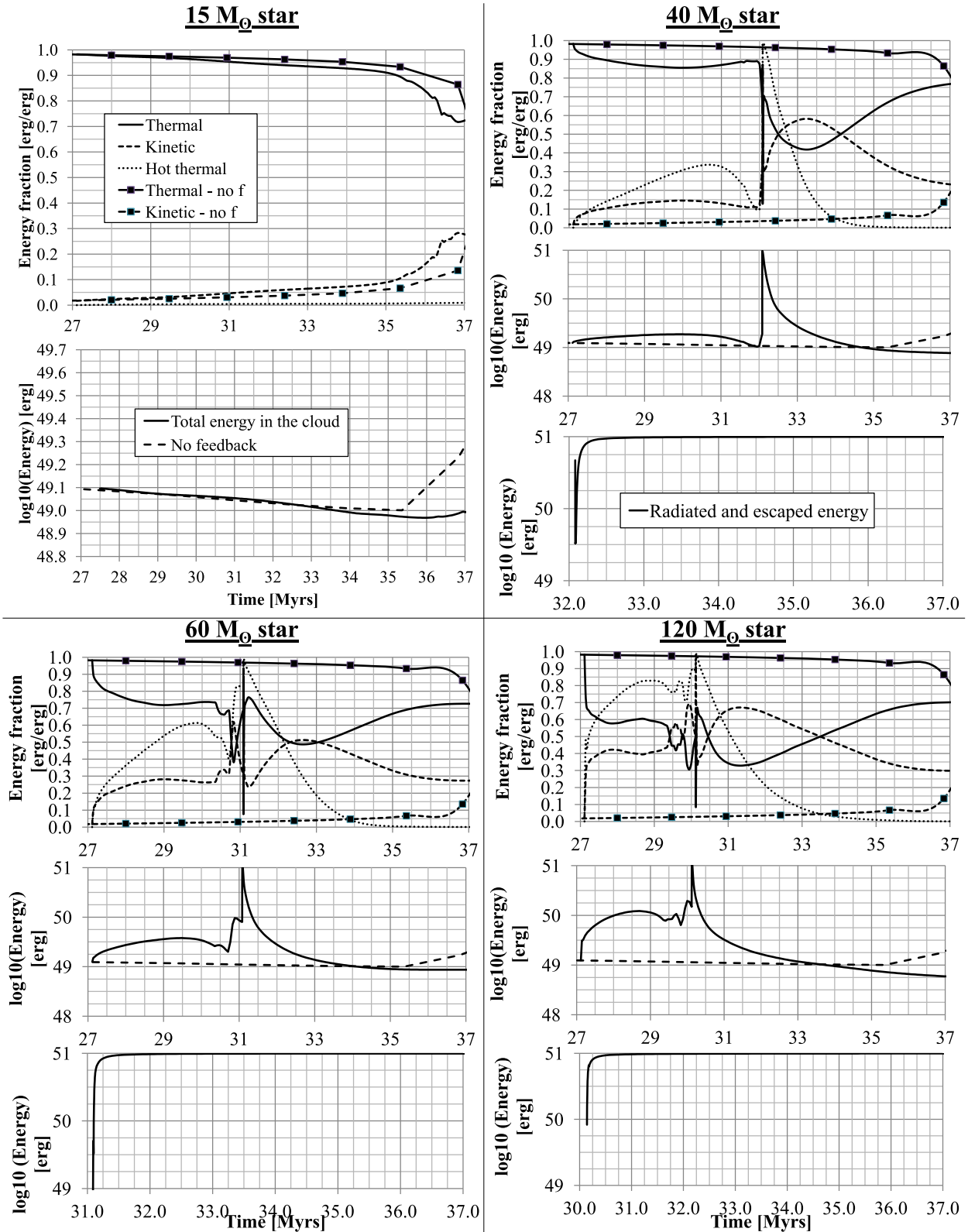
Figure 15. Time profiles of energy fractions, totals and escaped amounts of energy in the cloud, wind and SN material combined. The thermal and kinetic energy fractions together sum to 1.0, i.e. we are ignoring the change in gravitational energy. The 'hot thermal' profile indicates the fraction of the thermal energy that is hot (above 10^4 K), and so also has a range between 0.0 and 1.0. Lines with markers indicate the energy behaviour in the cloud with no stellar feedback. On the third row of the 40, 60 and 120 $M_\odot$ star plots, the 'radiated and escaped energy' is the total energy subtracted from the injected energy of the SN, 10^{51} erg. Note the different time-scales in these plots. Raw data: doi.org/10.5518/201.
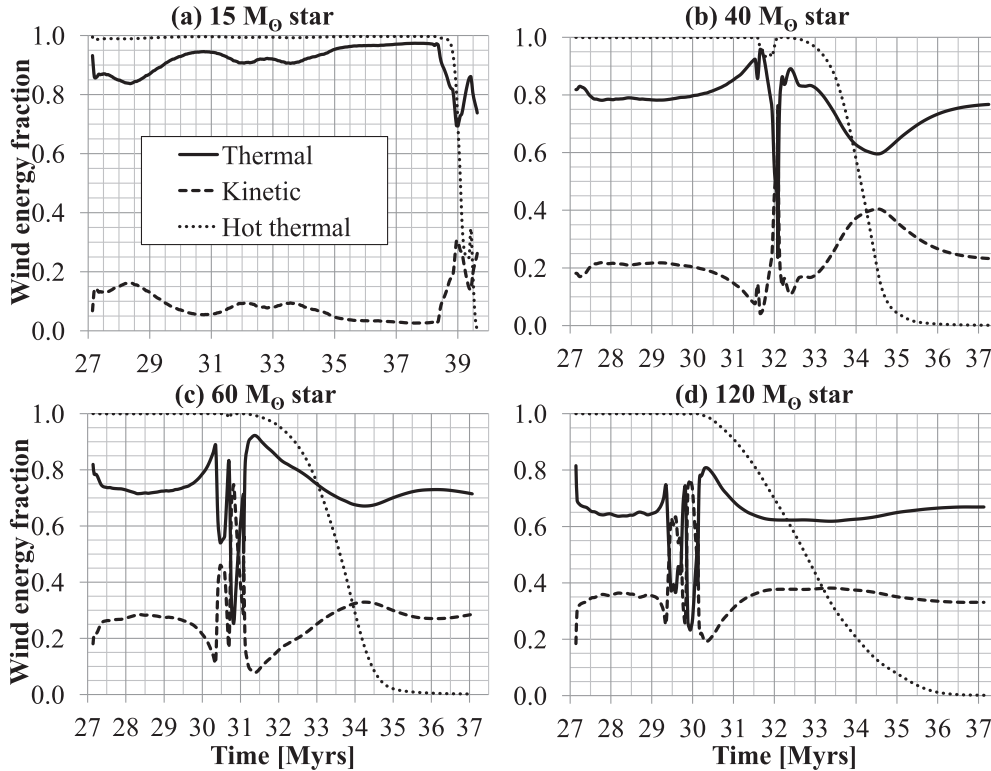
Figure 16. Time profiles of the energy fractions of the stellar wind material as traced by the advected scalar α_{wind}. The thermal and kinetic energy fractions together sum to 1.0, i.e. we are ignoring the change in gravitational energy. The 'hot thermal' profile indicates the fraction of the thermal energy that is hot (above 10^4 K), and so also has a range between 0.0 and 1.0. Raw data: doi.org/10.5518/201.

case though, the forward shock leaves the grid along the wind-carved channels much more quickly, first reaching the edge of the computational volume after only 15 000 yr. The initial peaks are followed by similar evolution between the thermal, hot thermal and kinetic energy fractions when compared to the 40 $M_\odot$ star case. The thermal energy plateau of warm, neutral medium is reached on the same time-scale. Whilst the detailed evolution of the cloud with feedback from a 60 $M_\odot$ star is visibly very different from the 40 $M_\odot$ star case, as shown in the previous section, the evolution of the energy fraction, total energy and radiated/escaped energy is not considerably different.

The 120 $M_\odot$ star case is similar to the case of the 60 $M_\odot$ star. The wind introduces considerably more kinetic energy though, driving shock heating and a greater fraction of hot thermal energy. The late stages of stellar evolution are equally complex and track the variations in energy injection rate, but the post-SN evolution is remarkably similar. Most interestingly, the SN from the 120 $M_\odot$ star very rapidly loses thermal energy post-SN and the kinetic energy peaks at a higher fraction than both the 40 and 60 $M_\odot$ star cases. Again, the forward shock leaves the grid in around 15 000 yr, along the low-density channels carved by the wind through the cloud and surroundings. Although the post-SN material in the 120 $M_\odot$ case does briefly plateau in the warm, neutral phase between 2.5 and 3.5 Myr post-SN, the thermal energy on the grid then continues to decrease. The grid is dominated by the hot, low-density void of the inner SNR, which is still cooling, leading to this effect. Any warm, neutral medium would be outside the grid. This highlights the range upon which each star acts, increasing with the mass of the star (and hence strength of the wind). A larger computational volume is clearly necessary to capture the characteristics of the surrounding medium that the 120 $M_\odot$ star creates post-SN.

In Fig. 16, we show the evolution of the energy fraction of stellar wind material for each star. The wind material injected by the 15 $M_\odot$ star is almost completely dominated by hot thermal energy, and has very little kinetic energy, until the end of the star's life (indicating that the wind is 'bottled up'). The wind material from the 40 $M_\odot$ star has a greater fraction of kinetic energy, which increases steeply close to the SN event as the star enters its WR phase. Post-SN, the energy of the wind material follows a similar trend to that of the total energy in the simulation, as shown in the last figure. The same trends are seen in the 60 and 120 $M_\odot$ star cases. In Fig. 17, we show the evolution of the energy fractions of the SN material for each star. Clearest in panel (a), showing the first few tens of thousands of years of the SNR evolution, is the initial conversion of thermal energy into the kinetic energy of expansion of the ejecta (causing the thermal energy to drop to only 10 per cent of the total ejecta energy), followed by a rapid increase to 35 per cent as the expanding ejecta passes through a reverse shock and is rethermalized to an 85 per cent fraction. Over the next 4 Myr, the thermal energy fraction drops to 60 per cent of the total (but since material is lost off the grid one cannot draw any further conclusions).

4.2 Maximum density

In Fig. 18, we show the maximum densities reached in the simulations, compared to the maximum density at the same time in the reference case without stellar feedback. In the 15 $M_\odot$ star case, the maximum density during the wind phase follows the reference case. The maximum density is more than 10^6 H cm^{-3} during the cloud collapse, realistic in the gravitational collapse of a molecular cloud, but beyond the accuracy of the resolution used in this simulation. In the other three cases, the stellar winds are able to create
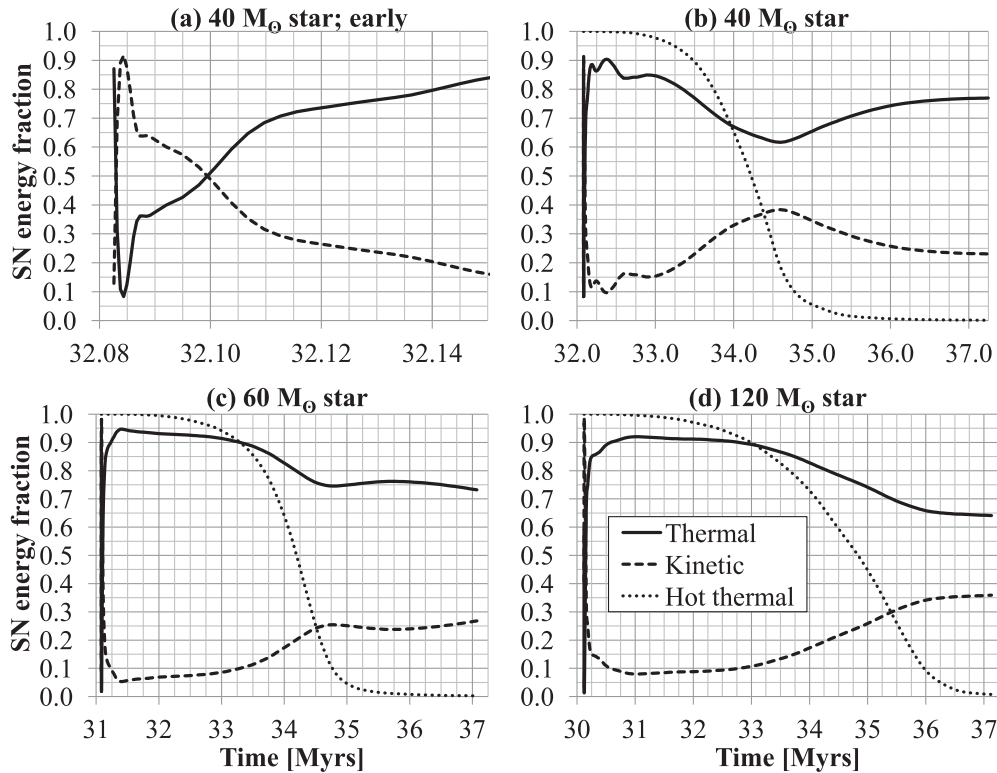
Figure 17. Time profiles of the energy fractions of the SN ejecta, as traced by the advected scalar α_{SN}. The thermal and kinetic energy fractions together sum to 1.0, i.e. we are ignoring the change in gravitational energy. The 'hot thermal' profile indicates the fraction of the thermal energy that is hot (above 10^4 K), and so also has a range between 0.0 and 1.0. Raw data: doi.org/10.5518/201.

considerably higher densities than in the reference case during the wind phase, enough for the possibility of a second generation of star formation with densities over 10^3 H cm^{-3}. Variations are not due to the stellar wind – it is relatively steady with smooth variation over the majority of the star's lifetime – but instead must be due to the compressional effect the stellar wind has on the cloud, rearranging the structure and compressing 'spokes'.

By the time of the SN, the maximum density in all three cases is back to similar levels to the reference case, showing that whilst the final wind stages inject a considerable amount of mass, densities elsewhere reduce as the cause of increased density, compression by the wind, has reduced. The SN instantly raises the density in the injection location, but the spikes seen in the plots are instead associated with compression of surrounding LBV/WR material and then cloud material in the 40 M$_\odot$ star case, and the cloud material in the 60 and 120 M$_\odot$ star cases. Later peaks in the maximum density plots, showing against the overall decreasing trend of maximum density, may be associated with the formation of new cold material after SN-affected material returns to the thermally unstable phase. Localized star formation, according to our star formation rules, would occur in all these cases. Only in the case of the 60 M$_\odot$ star is a late onset increase in maximum density apparent (post-34.5 Myr). This must be associated with increasing amounts of cold molecular material, even in the warm, neutral medium. This is investigated further in the next sub-section.

4.3 Phases

In Fig. 19, we show the phase fraction and total cloud mass for all four feedback simulations. At the injection of a star, 27 Myr

into the cloud's evolution, the cloud is in thermal equilibrium (i.e. on the equilibrium curve between heating and cooling processes) with 50 per cent of its mass in the warm phase (5000 K $\leq T \leq$ 10 000 K), $\approx$25 per cent of its mass in the cold phase ($T \leq$ 160 K) and $\approx$25 per cent of its mass in the unstable equilibrium part of the pressure–density distribution (160 K $\leq T \leq$ 5000 K). No material is in the hot thermal phase ($T \geq$ 10 000 K).

Once mechanical feedback starts the cloud material is shock heated out of thermal equilibrium and requires a cooling time to radiate away its excess energy. The low-density shocked stellar wind gas has a comparatively long cooling time-scale, while the denser and cooler swept-up gas has a much shorter cooling time-scale. Later on, the hot SN ejecta and the gas it sweeps up have comparatively long cooling time-scales.

Fig. 19(a) shows that during the wind phase of the 15 M$_\odot$ star case before the cloud collapses (beyond $t = 37$ Myr), the fraction of cold material decreases during the first 0.5 Myr, with a corresponding increase in unstable material, then slowly increases very much like the reference case with no feedback – the molecular cloud continues to form around the stellar wind bubble. The introduction of stellar feedback has little effect upon the amount of warm thermally stable material, until close to the collapse of the cloud. The presence of a larger quantity of unstable material as compared to the reference case enables the condensation of slightly more cold material, allowing the fraction of cold material to increase above the reference case with feedback. One of the very few effects of the 15 M$_\odot$ star then is to slightly increase the amount of cold molecular material in the cloud.

In panel (b) of Fig. 19, we show the phase evolution of the material in the simulation of mechanical feedback from the 40 M$_\odot$ star. The
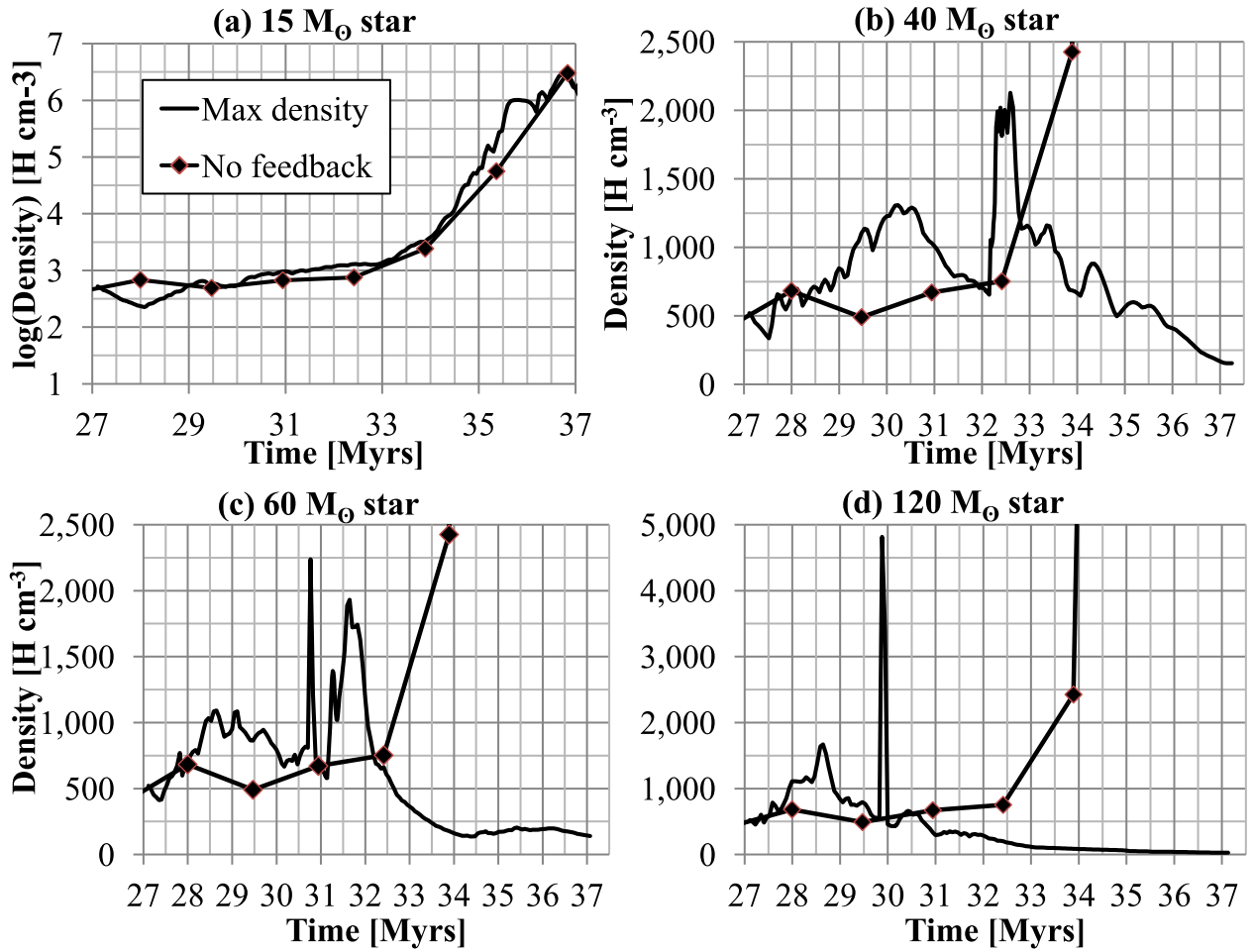
Figure 18. Maximum densities reached in the stellar feedback simulations (solid lines) shown with the maximum density in a continued simulation of the same initial conditions without feedback (lines with markers) for reference. Note that without feedback, the cloud collapses to unrealistic densities for the resolution of the simulation. The SN occurs at $t = 32.1$, 31.1 and 30.1 Myr for the $M = 40$, 60 and $120\,M_\odot$ cases. Raw data: doi.org/10.5518/201.

effect upon the cloud is greater than that of the 15 $M_\odot$ star. Whilst the warm fraction remains reasonably constant for the first 2 Myr, the stellar wind rapidly heats cold cloud material, moving it back into the unstable phase (from where it all originally began in the diffuse initial condition preceding the formation of the molecular cloud at $t = 0$). The unstable phase fraction increases and the cold phase fraction decreases. Over the rest of the star's life though, both the cold and unstable phase fractions continue to grow, at the expense of the warm phase, which drops to below 20 per cent by the time of the SN, compared to 50 per cent in the reference case at the same time. Clearly, the star reduces the amount of cold material formed in the cloud (to 30 per cent, rather than more than 40 per cent in reference case), but is not able to stop the cloud continuing to form cold material. The SN then transports hundreds and eventually thousands of solar masses of SN, wind and then cloud material out of the cloud. The SN rapidly heats nearly 10 per cent of the cloud material into the hot thermal phase (above 10 000 K), but the majority of this material radiatively cools quickly and the fraction of hot material drops back close to zero before the SNR leaves the cloud (from about 0.5 Myr after the explosion). The major effect of the SN is to transition nearly 70 per cent of the material on the grid into the thermally unstable phase, mostly from the warm phase. The amount of cold material also decreases very rapidly post-SN, returns

briefly to nearly 30 per cent after 0.5 Myr post-explosion – the point at which the SN forward shock has progressed through the cloud – and then decreases as the remnant evolves. These changes can be understood as the sweeping up and ejection of material from the cloud by the SN, whilst the cold cloud material reacts much more slowly. Some of this behaviour is also due to the (SN) shock heating and subsequent cooling of dense material, as found by Rogers & Pittard (2013). The fraction of cold dense material remains at around 20 per cent throughout the post-SN evolution, with a slight increase at late time, matched by an increase in warm phase material, with the unstable phase feeding into both. Cold molecular components are still present in the simulation, albeit at a 20 per cent fraction rather than the 50 per cent fraction seen without feedback. They have not been destroyed by the SN, even if the structure of the cloud has been disrupted. It should be noted though that this result is at the limit of applicability of these simulations, as numerical issues are present due to the forward SN shock having long since passed off the grid.

In the case of the 60 $M_\odot$ star, we observe many similarities to the case of the 40 $M_\odot$ star. The 120 $M_\odot$ star also shows similar changes, though they are more extreme, during the stellar wind phase, with less than half the cold phase material present by the time of SN, as compared to the reference case, and less than all the
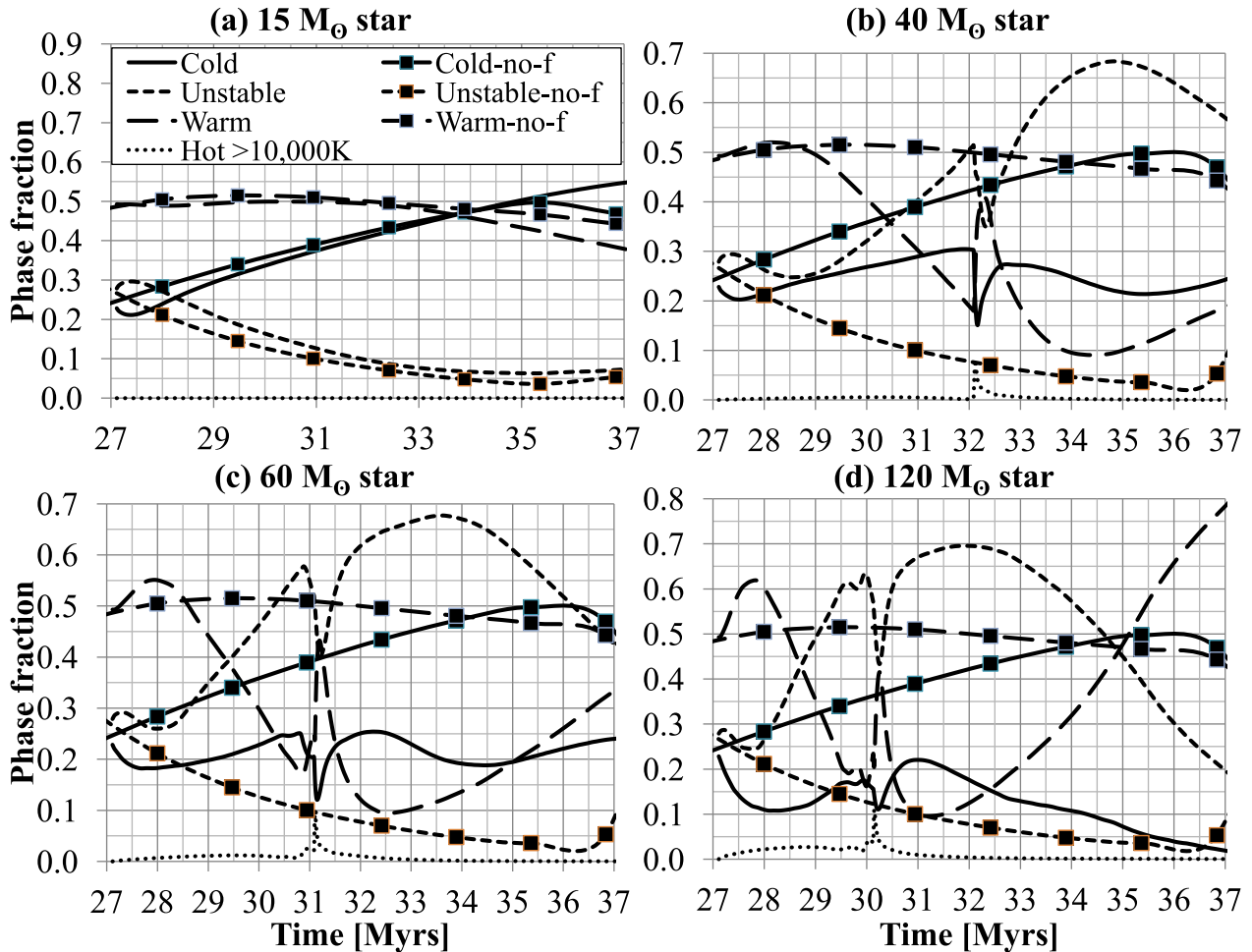
Figure 19. Variation of phase fractions with time for the feedback simulations. The reference case without feedback is indicated by lines with markers in the phase fraction plots. Raw data: doi.org/10.5518/201.

other cases. An appreciable fraction of hot thermal phase material is also present, around 5 per cent by the time of SN. After the SN, the first Myr is also similar to the preceding cases, but after that the evolution is markedly different from the preceding cases. There is no levelling off of the cold phase fraction, never mind an increase. By the end of the simulation, less than 5 per cent of the material in the computational volume is in the cold phase. The volume is completely dominated by warm phase material – nearly 80 per cent of the total material present – with the remainder in the unstable phase. This is most likely because of the combined strength of the stellar wind and subsequent SN that completely destroy the parent molecular cloud. Any remaining cold molecular material has been blown out of the computational volume. We can therefore state that it takes more than a 60 M$_\odot$ star to completely disperse a molecular cloud by mechanical feedback under these conditions, but that a 120 M$_\odot$ star is very efficient at this dispersal.

In Fig. 20, we plot the mass-weighted temperature–density (in the left column) and pressure–density (in the right column) distributions for the four cases considered in this work, using 200 bins in log density and 200 bins in log temperature/pressure. We also overplot the approximate thermal equilibrium curve for the heating and cooling prescriptions used in this work. In the first row, we show the distributions 10.97 Myr through the wind phase for the case of the 15 M$_\odot$ star, shortly before complete cloud collapse. Most of the material remains in thermal equilibrium, tracing the equilib-

rium curve. The two distinct stable phases (warm and cold) are, as expected, in approximate pressure equilibrium with each other. A low-density, higher temperature stellar wind bubble (as shown in the bottom row of Fig. 4) is indicated by the branch stretching away from the equilibrium curve horizontally to the left at the same $P/k \sim 10^{3.8}$ K cm^{-3} in the pressure–density distribution.

In the second row of Fig. 20, we show the distributions for the case of the 40 M$_\odot$ star at the end of the wind phase. The distributions have the same components on the equilibrium curve that are present in the case of the 15 M$_\odot$ star, but there are also other considerable regions. We can identify branches from gas in the wind bubble and the LBV/WR shell. The lower pressure horizontal branch at $P/k \sim 10^3$ K cm^{-3} is the wind bubble, at notably lower pressure and temperature than the previous case. The LBV/WR shell that formed during the last stages of stellar evolution is responsible for the branch and arc of material out of equilibrium at higher pressure. Specifically, the diagonal line that spans from $(\log(P), \log(\rho)) = (6, -1)$ down towards the tunnel branch at $(\log(P), \log(\rho)) = (3, -3)$ is the wind injection region and region of undisturbed wind material up to the reverse shock. The reverse shock is indicated by the jump back up in pressure to the overpressured (with respect to the cloud and other wind bubble tunnel) LBV/WR shell that is itself indicated by the horizontal branch at $P/k \sim 10^5$ K cm^{-3} that arcs back to the equilibrium curve, broadening as it cools and increases in density. The greater power of the wind has also driven a broadening
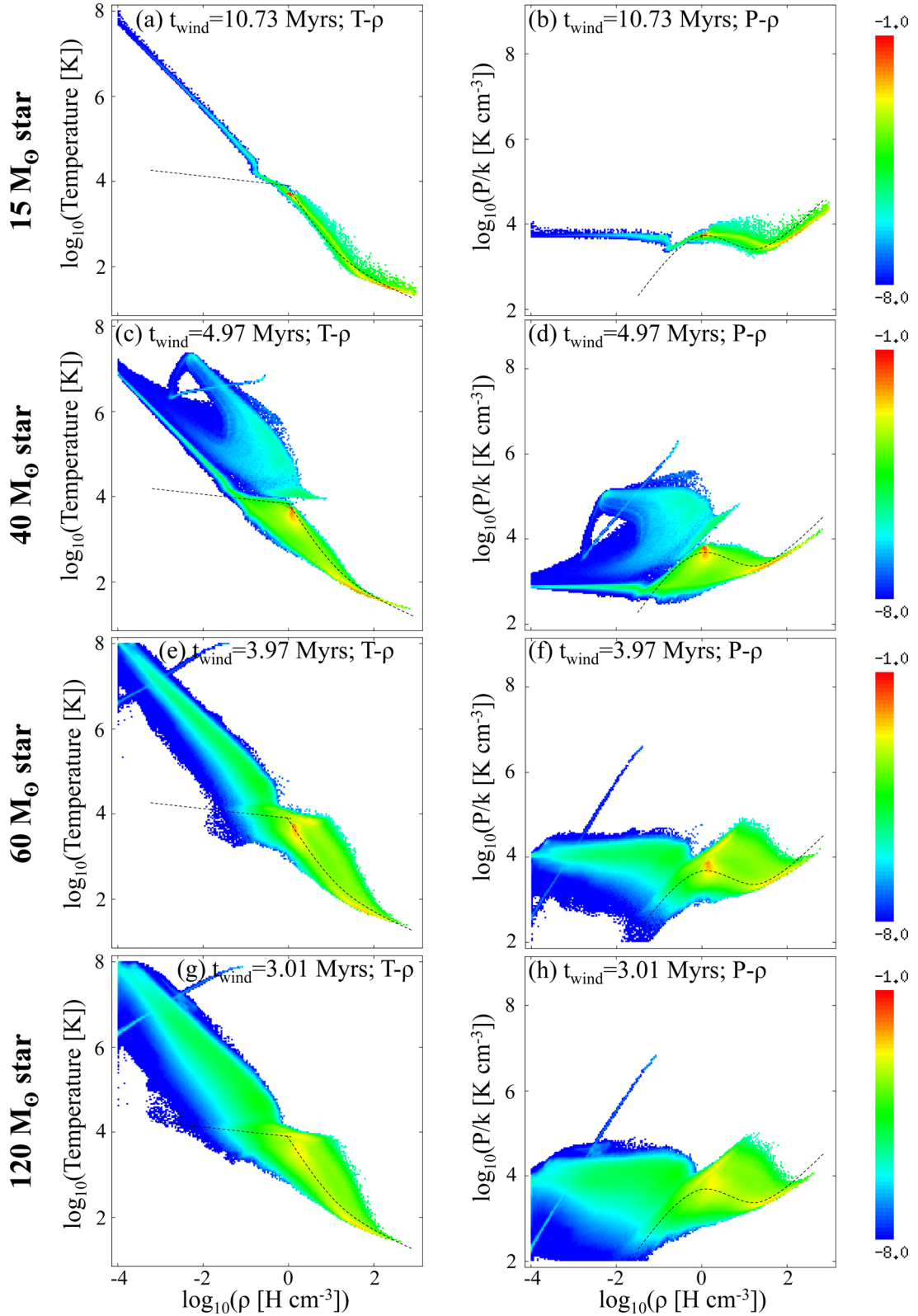
Figure 20. Mass-weighted temperature–density and pressure–density distributions at the end of the star's life for each of the simulations. Overplotted dashed lines indicate the approximate thermal equilibrium between heating and cooling for the prescriptions used. Raw data: doi.org/10.5518/201.

of the distributions, with heated material above the equilibrium curve radiatively cooling towards the equilibrium curve. Cooling by expansion has led to low-density, cool gas below the equilibrium curve. The distributions in this case are very similar to the case of the

$40\,M_\odot$ star in Paper II, despite the marked difference in structures: a bubble in a clumpy cloud here, a tunnel through a filamentary sheet there. Common to both cases and responsible for much structure in these distributions is the LBV/WR shell structure. Looking at the
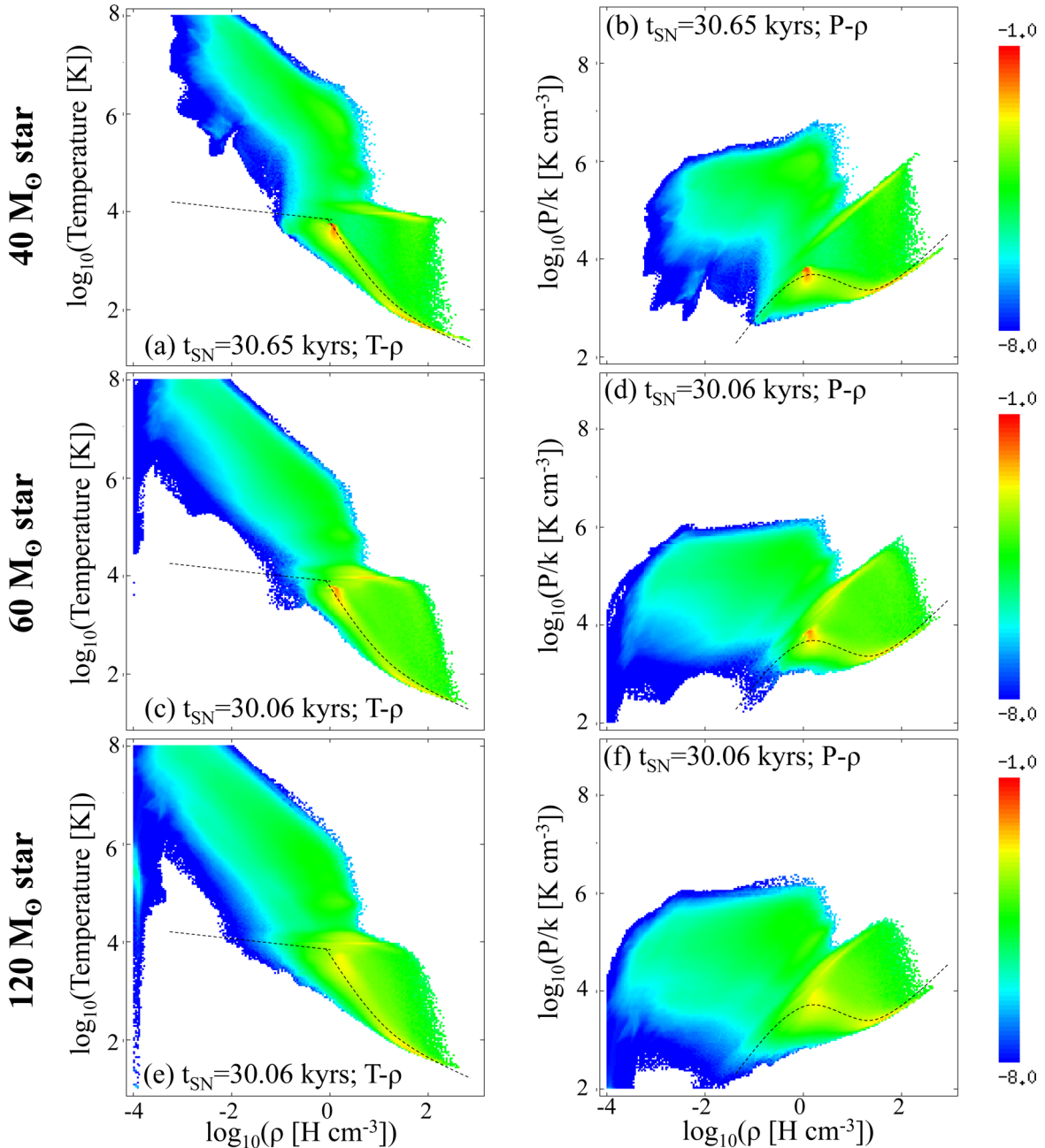
Figure 21. Mass-weighted temperature–density and pressure–density distributions for the simulations presented here during the early evolution of the SN in each case. Overplotted dashed lines indicate the approximate thermal equilibrium between heating and cooling for the prescriptions used. Raw data: doi.org/10.5518/201.

distributions, it is impossible to discern the considerably different overall wind-cloud structure responsible for each. It may be possible to conclude that lower pressure wind branches are indicative of larger, less confined structures.

The third and fourth rows of Fig. 20 show the distributions for the cases of the 60 and 120 $M_\odot$ stars and are remarkably similar. Both contain isolated diagonal lines that are again indicative of the wind injection regions and regions of undisturbed WR wind material up to the reverse shock. In both cases, the jump back up in pressure at the reverse shock is at, or just off, the lower density axis boundary of each figure, as can in fact be seen at low density in Figs 6 and 7. The greater power of the winds and merger of the LBV/WR

material with the whole wind bubble has created a single, broader distribution, pushing more and more material out of equilibrium, until in the case of the 120 $M_\odot$ star, most of the material is out of equilibrium.

In Fig. 21, we show the distributions 30 kyr after the SN for the three simulations with SNe. Towards the upper left of each distribution is the low-density, hot phase, which consists of SN shock-heated gas. It is not yet in pressure equilibrium with the warm phase, but evolves towards this equilibrium as the simulation progresses beyond that shown here. The distribution at low density is reasonably wide in pressure and temperature and widens with increasing stellar mass. The reason for this is the presence of both shock-heated and

adiabatically cooled gas, as noted in a similar analysis of such distributions influenced by feedback simulated by Walch et al. (2015). The SN has also shock heated an appreciable amount of the cold dense material, spreading the distribution upwards at high density in all three plots.

In Fig. 22, we show the mass-weighted temperature–density and pressure–density distributions at late times after the SN for the case of the 60 M$_\odot$ star. We can see the broad distribution is cooling (shifting downwards) in both plots. The material is also moving back towards thermal equilibrium, and by 4.5 Myr post-SN essentially all the material is back in thermal equilibrium. The evolution of the 40 and 120 M$_\odot$ star cases is very similar, albeit with lower amounts of high-density material and lower maximum densities in each case (i.e. less material on the right of equivalent plots to those shown in Fig. 22).

4.4 Total cloud mass

In Fig. 23, we show the variation of total mass in the computational volume with time for the case of each star. The reference case is not shown, as it overlaps the 15 M$_\odot$ star case, highlighting again the little influence of the 15 M$_\odot$ star. In the 40 M$_\odot$ star case, the total mass remains approximately the same until the SN (at 32.1 Myr), when the SN event drives mass out of the computational volume. The wind phase of the 60 M$_\odot$ star drives a few hundred solar masses of material out of the computational volume, before the SN (at 31.1 Myr) expels considerably more mass. In both the 40 and 60 M$_\odot$ star cases, the majority of mass remains on the grid post-SN until beyond the end of the simulations. Most of it is out of equilibrium in the thermally unstable temperature range, as revealed by the preceding plots in this sub-section. Even by the time of SN (at 30.1 Myr), the wind from the 120 M$_\odot$ star has already driven nearly 2000 M$_\odot$ of material out of volume – more than 10 per cent of the cloud's original 16 500 M$_\odot$. Most of this expulsion occurred during the stellar evolution off the main sequence, during the final Myr or so of the star's life. The expulsion of mass continues during the SN phase, until 6 Myr post-SN, only 20 per cent of the initial mass remains in the simulation. As such, the cloud has been effectively dispersed and a larger simulation is required to track the final properties of this material. This would suggest that whilst the star has destroyed the cloud and replaced it with a tenuous warm phase SNR surrounded by warm medium, some cold material may have survived the violent evolution of the 120 M$_\odot$ star, but is now entirely separate from its origins in the parent molecular cloud.

In Fig. 24, we show the variation of mass gravitationally bound to the potential of the cloud in the computational volume with time for the case of each star. That is, we show the amount of mass within the gravitational potential well of the original cloud that does not have enough kinetic energy to escape the gravitational potential of the cloud. Here is the only place the 15 M$_\odot$ star has an appreciable effect over the reference case, although by the end of the star's evolution, the amount of gravitationally bound mass has returned to the same level as the case without feedback. In the 40 M$_\odot$ star case, the main-sequence evolution of the star provides enough energy for nearly half the mass of the cloud to overcome the gravitational energy and either leave the domain or have enough kinetic energy to overcome the gravitational potential, but the late stages of evolution increase the amount of mass associated with the cloud. The effect of the SN is to disperse the remainder of cloud, although 2 Myr after the SN, the amount of gravitationally bound mass is increasing again, indicating that the increasing levels

of cold material noted previously are now bound to the cloud itself. The 60 M$_\odot$ star shows a similar, but more disruptive pattern, with the cold molecular material formed more than 2 Myr post-SN now associated with the cloud. There is considerably less material in this case. The 120 M$_\odot$ star is able to completely disperse the cloud material during the star's lifetime ($\sim$3 Myr), confirming the conclusions drawn above. No increase post-SN is noted.

4.5 Mixing

In Fig. 25, we show the mixing of the stellar wind material with cloud material. In the 15 M$_\odot$ star case, wind material is immediately well mixed and remains that way, since it is all at fractions of no higher than 20 per cent with respect to the cloud material. Whilst an equivalent amount of material to the star's mass was taken out of the injection region to make the star, some cloud material remained in the injection region and the wind material was introduced as a source term adding to this; hence, the wind material mixed very quickly. There is no brief period when the injection region is almost entirely wind material, i.e. there is no transition observed from 'no mixing' (at 100 per cent) down to well mixed. Therefore, the initial few thousand years of stellar wind may be quite effectively quenched, but this is a transitory period and outweighed by the benefit of using a source term rather than an imposed wind structure in those cells, which tests and previous experience (e.g. Wareing, Zijlstra & O'Brien 2007, and other works therein) have shown can impose grid-based structure upon the resulting wind. The wind from the main-sequence phase of the 40 M$_\odot$ star is almost as well mixed as that of the 15 M$_\odot$ star. In this case, the brief initial period of mixing down from almost 100 per cent in the injection region is indicated by a very small initial peak, due to the stronger stellar wind. However, the final 0.5 Myr of stellar wind injection shows the isolated and unmixed nature of the LBV/WR shell, and also how much material is in the shell, given the height of the peak. At 32.08 Myr, the SN explodes and in short time mixes the wind material down to concentrations of below 20 per cent wind material. Both the 60 and 120 M$_\odot$ star cases show peaks of unmixed material in the final stages of stellar evolution, but with decreasing levels, down to the 120 M$_\odot$ star case where the majority of wind material remains efficiently well mixed throughout the star's lifetime, albeit with larger fractions of other levels of mixing than in any of the other cases. Peaks and troughs in the final stages of stellar evolution can be attributed to the different phases of the stellar wind and transitory shells that arise during these stages. The effect of the SN on the mixing of wind material is similar and is very efficient in all cases.

In Fig. 26, we show the mixing of SN material with cloud and wind material in the three SN cases presented in this work. In panel (a), we focus upon the early mixing of the SN ejecta, in the first few hundred thousand years following the explosion of the 40 M$_\odot$ star. Initially, all the SN material is unmixed (80–100 per cent), remaining so for a few thousand years and then is slowly mixed down into the more mixed brackets in this figure. Within 0.1 Myr though, the SN material is efficiently mixed down to 0–20 per cent fractions within the cloud/wind material. At later times, the SN material continues to remain well mixed. Mixing is more efficient, taking less time to completely reach the 0–20 per cent brackets for the more massive stars.

For these simulations, as for those in Paper II, we have not quantitatively examined the nature of the material leaving the grid. In the three more massive cases, the SN drives material out of the cloud, as investigations of the phase fractions of material have shown.
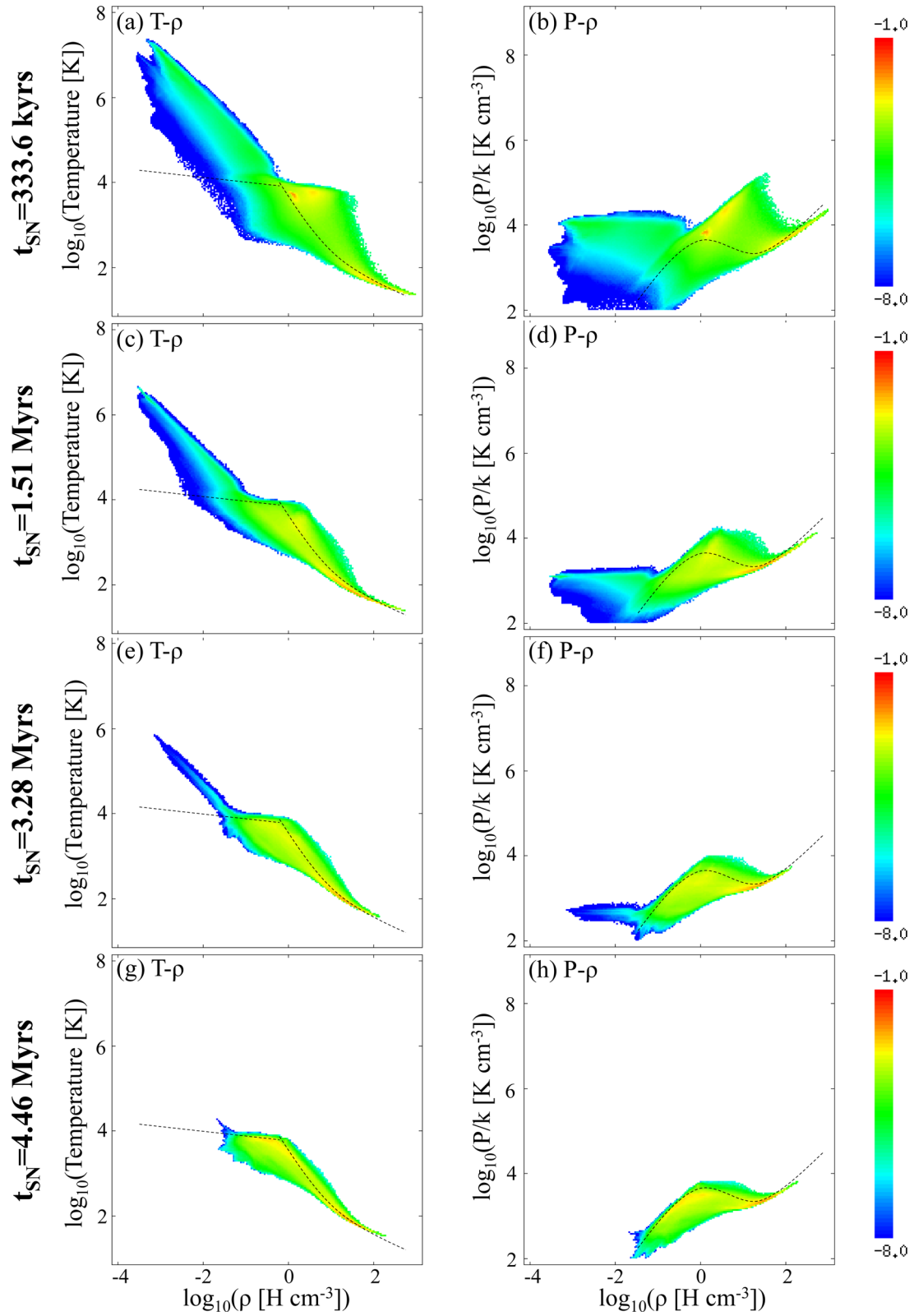
Figure 22. Mass-weighted temperature–density and pressure–density distributions for the 60 M$_\odot$ star case in the late stages of the SN event. The evolution of the 40 and 120 M$_\odot$ star cases are very similar. Overplotted dashed lines indicate the approximate thermal equilibrium between heating and cooling for the prescriptions used. Raw data: doi.org/10.5518/201.
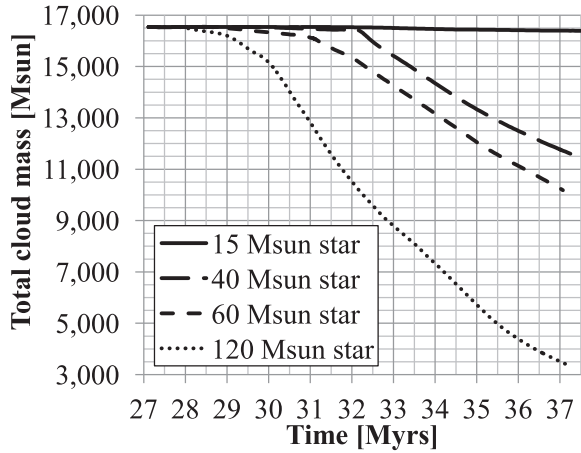
Figure 23. Variation of total mass in the computational volume with time for the feedback simulations. The reference case without feedback is not shown, but almost precisely overlies the 15 M$_\odot$ star case. Raw data: doi.org/10.5518/201.
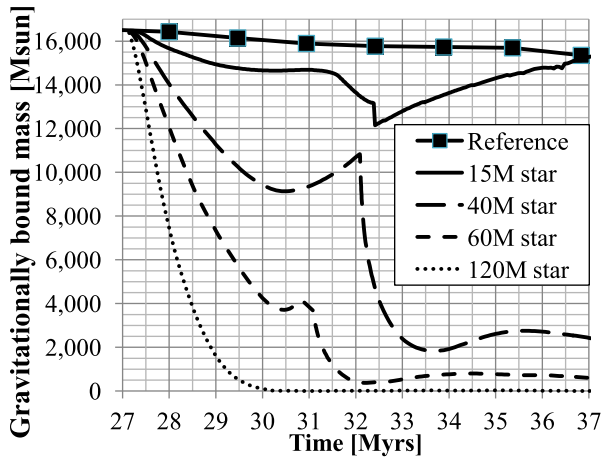

Figure 24. Variation of gravitationally bound mass (i.e. kinetic energy plus gravitational energy is less than zero) in the computational volume with time for the feedback simulations. Raw data: doi.org/10.5518/201.

Further investigations may shed more light on mass loading and the entrainment of material leaving the grid.

5 DISCUSSION

5.1 Comparisons to previous work

Comparing the present work with our previous efforts in the hydro-dynamic case (Rogers & Pittard 2013, 2014) is not straightforward due to the large differences in initial conditions. However, there are some clear similarities. In both, the later wind energy and SN energy are transferred to the wider surroundings through a multitude of porous channels. In Rogers & Pittard, this was as a result of the imposed initial condition and was associated with a much higher density filamentary cloud in a smaller volume. Here, the early phases of the stellar wind result in similar channels and gaps, even though the initial condition is that of a clumpy cloud with no filamentary network. This finding, of clear gaps and channels carved out through parental molecular clouds, would appear to be a common evolutionary conclusion when mechanical feedback from stars is involved. Only when a magnetic field is present, effectively

focusing the outflow from a massive star into a single channel as we found in Paper II, are the results morphologically and quantitatively different. Nevertheless, it is clear that winds are on the whole quite capable of breaking out of their confining clouds. Such leakage of the hot gas is consistent with the much lower mass of hot cluster gas than expected for the cluster ages and the mass-loss rates of stars (Townsley et al. 2003) and by energy budget considerations (Rosen et al. 2014).

In common with Rogers & Pittard, the densest molecular regions are surprisingly resistant to ablation by the stellar/cluster wind. In both works, this is partially due to shielding by other dense regions closer to the star/cluster. Pressure gradients within the flow appear to rearrange the molecular cloud structure into radially aligned spokes or filaments, so that the head of the spoke closest to the star shields the remainder of the structure. Further simulations are required to investigate whether this behaviour extends to clumpy clouds of higher mass and density.

In common with all our previous work, SNe are able to transport large amounts of energy directly out of the parent cloud, with existing channels and gaps allowing weaker coupling to the remaining dense material. Such channels are further carved out by the SN. The key factor is the shaping effect of the pre-SN stellar winds, which make the cloud highly porous (Rogers & Pittard 2013, and the current paper), or as in Paper II where they are focused by magnetic fields to open up large-scale channels directing SN energy out of the cloud. In all cases, the winds appear to be better at removing molecular material from the cloud/cluster environment, despite typically injecting less energy than the SN(e). The molecular material in all cases was found to be almost completely removed from the original cloud after 6 Myr post-SN. These works together demonstrate the complexity of the interaction of a stellar wind with an inhomogeneous environment. The results are far removed from simple spherically symmetric models and compare nicely with the simulations of Geen et al. (2016) who argue that strong pre-SN (radiative) feedback is required to allow SN blastwaves to propagate efficiently into the ISM.

A key common finding between this work and Paper II is that lower mass stars (15 M$_\odot$ or less) have little global effect on the parent cloud. Here we find that the weak wind is unable to overcome the gravitational collapse of the cloud. In Paper II, the local small bipolar wind bubble is eventually refilled by the slow wind from the late stages of the star's evolution, as we also note here. The effect in both cases is as if the stellar wind had not been present at all.

Harper-Clark & Murray (2009) considered stellar wind feedback into an inhomogeneous environment and postulated that the non-uniform surrounding medium causes gaps in the swept-up shell surrounding the wind-blown bubble where some of the high-pressure gas in the bubble interior can leak out. We have simulated a scenario very similar to this, with a stellar wind expanding into a non-uniform, inhomogeneous clumpy cloud. For the intermediate-mass cases (stars of mass 40 and 60 M$_\odot$), we find exactly that – the wind shell is non-spherical and has gaps or channels through it that allow gas to vent or blow out of the parent cloud. In the case of the 15 M$_\odot$ star, this effect is far less pronounced – the bubble that forms remains close to the star (within 10 or so parsecs) and no gaps or channels are seen around or outside the bubble. At the other extreme, the wind bubble around the 120 M$_\odot$ star destroys half the cloud by the end of the wind phase, and channels are present through the remaining cloud. In this case, dramatic structural changes occur within the cloud near the end of the star's life due to the increasingly powerful wind blowing at this time.
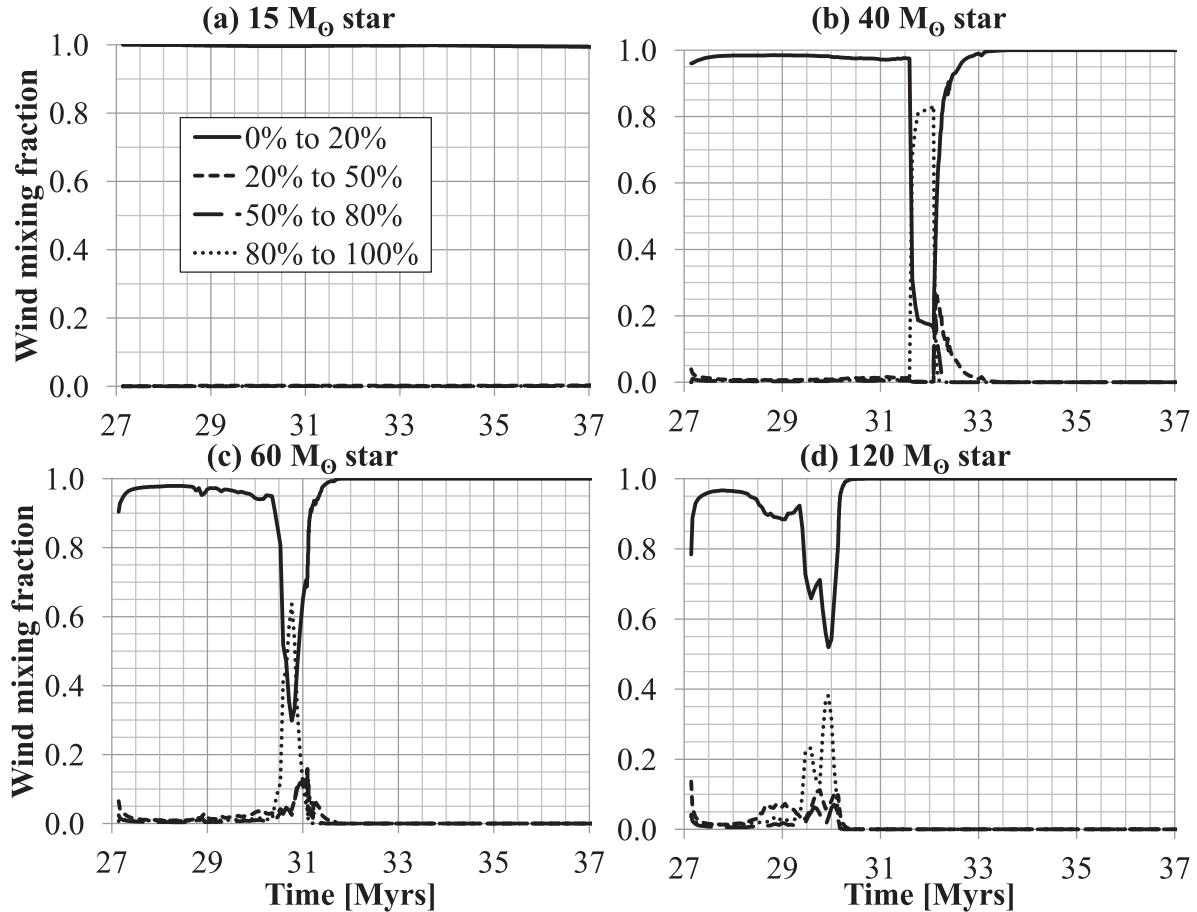
Figure 25. Levels of mixing of the wind material with the cloud material throughout the stellar feedback simulations. A value of 100 per cent indicates no mixing of the wind material with the cloud material. Raw data: doi.org/10.5518/201.

The effect of stellar winds on molecular clouds has also been considered by Dale et al. (2015) and Offner & Arce (2015). These simulations used either momentum-driven or isothermal winds and so give a lower limit to their impact. With this in mind, Offner & Arce (2015) concluded that stellar mass-loss rates for individual stars must be greater than 10^{-7} M$_{\odot}$ yr^{-1} in order to reproduce shell properties. As we noted in Paper II, the mass-loss rates for the 15 M$_{\odot}$ star are less than 3×10^{-7} M$_{\odot}$ yr^{-1} this limit for the entire main-sequence evolution of the star (see fig. 2 of Paper II). When the mass-loss rate exceeds this limit, the star is in its RSG phase, so the wind is slow and has little power. On the other hand, the higher mass stars always have mass-loss rates above this limit (as shown in Figs 2 and 3 of the current paper and fig. 3 of Paper II). Therefore, our findings are not in disagreement with Offner & Arce (2015), although we have not tested stars with masses between 15 and 40 M$_{\odot}$. The wind from the 15 M$_{\odot}$ star has little effect on the parent cloud, restricted to a 10 pc radius around the star. In contrast, the winds from higher mass stars strongly affect the parent molecular cloud.

Numerous recent works have explored the effects of SNe on the multiphase ISM and parent molecular clouds (e.g. Gatto et al. 2015; Körtgen 2015; Walch & Naab 2015; Walch et al. 2015; Girichidis et al. 2016; Körtgen et al. 2016). However, there is still much disagreement on the ability of SNe to drive outflows. For instance, Girichidis et al. (2016) found that strong outflows were only generated when SNe were randomly positioned and had the opportunity to inject energy into relatively low density environments. SNe placed at

density peaks instead radiate away too much energy to drive any noticeable outflow. However, they did not account for the effect of the SN-preceding stellar wind. In contrast, Simpson et al. (2016), who accounted for the production of cosmic rays in SN events, showed that outflows can be driven from SNe placed at density peaks. They found that their outflows have similar mass loading as obtained from random placement of SNe with no cosmic rays. Körtgen et al. (2016) find that single SNe disperse ~10-pc-sized regions but do not disrupt entire clouds, which instead requires clustered, short-interval SNe to form large hot bubbles. This is in contrast to our findings, but in mitigation our simulations focus on feedback in a cloud of lower mass than the Walch & Naab (2015) and Körtgen et al. (2016) studies, and also include the effect of the stellar wind, so it is not unexpected that our conclusions are somewhat different. Compared to these other works, our simulations clearly show that when stars are placed at high-density locations, their stellar winds can create gaps and carve channels out of the clumps and the parent cloud, allowing wind material and SN material to escape easily from the cloud, mass-loaded with material stripped from clumps in the parent cloud [Fierlinger et al. (2016) also find that pre-SN feedback enhances the impact of SNe]. Thus, the prior influence of winds should be included in simulations involving SN feedback.

5.2 Comparison to observations

Lopez et al. (2011) support the scenario presented by Harper-Clark & Murray (2009), concluding that leakage through gaps in the
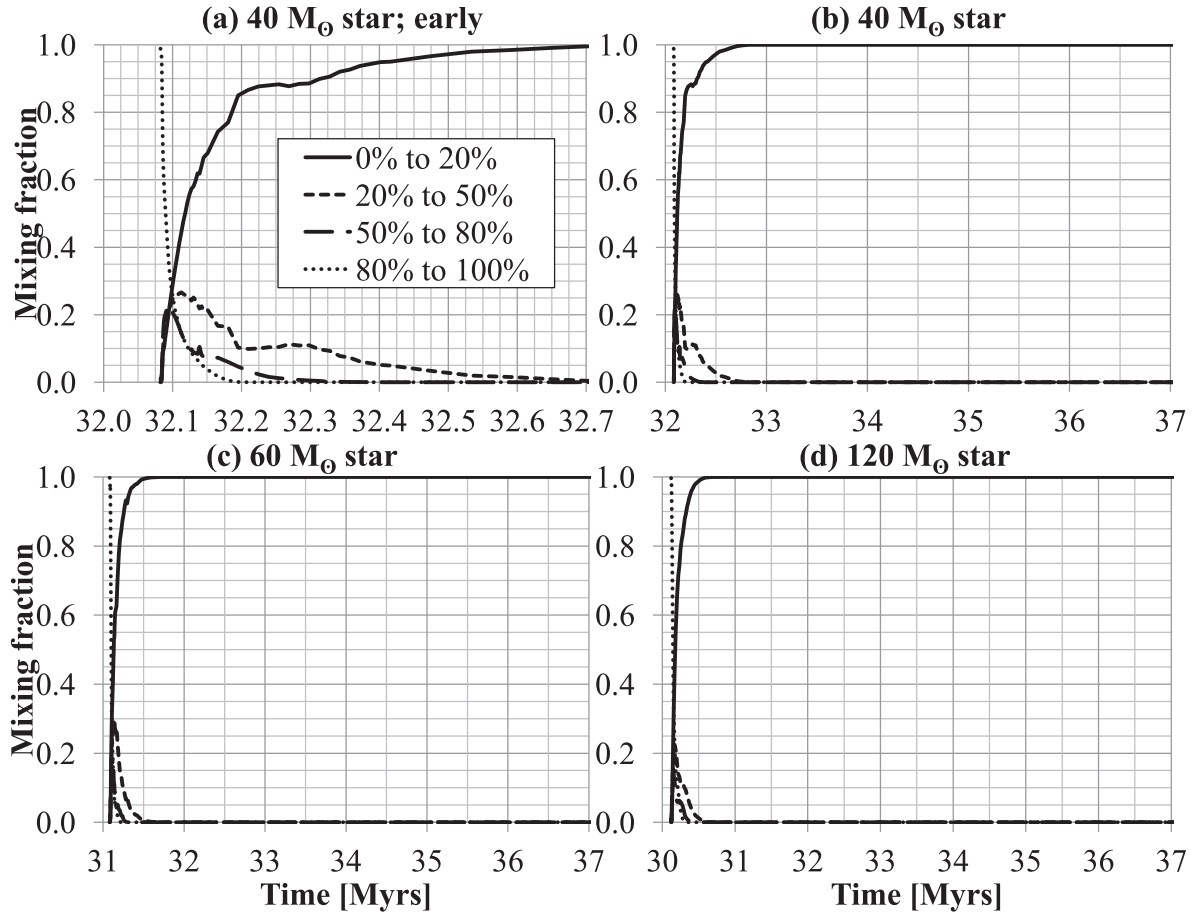
Figure 26. Levels of mixing of the SN material with the cloud/wind material throughout the stellar feedback simulations. A value of 100 per cent indicates no mixing of the SN material with the cloud/wind material. Raw data: doi.org/10.5518/201.

swept-up wind-blown bubble may be occurring within 30 Doradus. They claim that the lower X-ray gas pressure relative to the direct radiation pressure suggests that the hot gas is only partially confined and is hence leaking out of 'pores' in the H II shell. They also conclude that the significant radiation pressure near the central star cluster indicates that direct stellar radiation pressure dominated the interior dynamics at earlier times, but this claim has proved far more controversial, and other works are in favour of the thermal pressure of hot X-ray emitting plasma shaping the large-scale structure and dynamics in 30 Doradus. For example, Pellegrini, Baldwin & Ferland (2011) find that the dynamics and large-scale structure of 30 Doradus are set by a confined system of X-ray bubbles in rough pressure equilibrium with each other and with the confining molecular gas. In both the 60 and 120 M$_\odot$ cases presented herein, we find a structure of wind and cloud material in rough pressure equilibrium, as shown in Fig. 20. The existence of low-density channels carrying hot wind material is also clear from Figs 5 and 7. The more powerful the wind, the larger the cavity, the quicker the channels form and the wider they are, implying that a cluster of stellar winds will rapidly form multiple wide channels through a low-mass parent molecular cloud such as studied here. However, to determine whether hot gas thermal pressure or direct radiation pressure is dominant requires simulations with both mechanical and radiative feedback included.

Lopez et al. (2014) further assessed the role of stellar feedback at intermediate scales of 10–100 pc. They studied a sam-

ple of 32 H II regions (with ages from 3 to 10 Myr) in the Large and Small Magellanic Clouds and found that warm ionized gas dominates the dynamics whilst the hot gas pressures are comparatively weak. They emphasize that younger, smaller H II regions should be studied to elucidate the roles of hot gas and direct pressure in the early evolution of these regions. They also conclude that the hot gas is only partially confined in all of their sources, and suggest that hot gas leakage is common. Our simulations are by design influenced only by hot gas pressure, but nevertheless create the kind of structures observed by Lopez et al. (2014) and others.

It is also interesting to note the existence of structures within H II regions. For example, in RCW 120, arcs of dust emission are clearly seen within the H II region bubble in mid-IR *Spitzer* data. Mackey et al. (2016) interpret this as the outer edge of the wind-blown bubble. An alternative viewpoint is that dust arcs are waves induced by photoevaporation flows inside H II bubbles (Ochsendorf et al. 2014). Our simulations, although not able to define the extent of the H II region, do show complex structure within the wind bubble itself, for example bow shocks and LBV/WR shells, which could perhaps also lead to such observed structures. Such arcs could also be related to the aligned radial structures formed in the simulation of the 60 M$_\odot$ star. Photoionization of the complex structures formed by the 60 and 120 M$_\odot$ stars is bound to show one-sided H II regions too, as the stellar wind has blown out the molecular cloud in unequal measure around the star, as shown in Fig. 8.

Some H II regions (e.g. RCW 79, RCW 82, RCW 120) show a central hole in the 24 μm emission (e.g. Martins et al. 2010), which may also be evidence of stellar winds. However, these holes could also have been produced by radiation pressure. Simulations by Freyer, Hensler & Yorke (2003, 2006) show that stellar winds can have important dynamical effects even when the ratio of the injected wind to ionizing photon energy is as low as 0.01, but it is not known if this remains true at still lower ratios.

Two 'smoking guns' that reveal strong evidence for the potential impact of stellar winds are bow shocks around stars on the periphery of stellar clusters (e.g. Winston et al. 2012), and diffuse X-ray emission within and around young pre-SN clusters (e.g. Gudel et al. 2008; Townsley et al. 2014). However, it is clear that further observational and theoretical work is needed for a better understanding of the dynamics of H II regions and wind-blown bubbles/cluster outflows.

6 SUMMARY AND CONCLUSIONS

In this work, we have explored the effects of mechanical stellar wind and SN feedback on realistic molecular clouds without magnetic fields. Our initial condition has been based on the work of Wareing et al. (2016) in which a diffuse atomic cloud was allowed to form structure through the action of the thermal instability, under the influence of gravity, but without injected turbulence. The resulting structure is best described as a clumpy near-spherical cloud of approximately 100 pc diameter surrounded by a diffuse atomic cloud, when we introduce mechanical stellar feedback. The clumps are roughly equally distributed over the inner region of the cloud ($r \leq 50$ pc) when the densities in some clumps reach 100 cm^{-3}. A single massive star was then introduced at the highest density location closest to the centre of the cloud. We considered four cases: formation of a 15 M$_\odot$ star, a 40 M$_\odot$ star, a 60 M$_\odot$ star and a 120 M$_\odot$ star. Their stellar winds (based on realistic Geneva non-rotating stellar evolution models) subsequently affect the parent cloud, and at the end of life of the three highest mass stars an SN explosion is modelled. We do not model an SN explosion in the case of the 15 M$_\odot$ star as the cloud collapses under gravity before the end of the star's life and the simulation loses meaning at the resolution available.

In the 15 M$_\odot$ star case, the stellar wind has very little effect on the molecular cloud, and forms only a small cavity around the star that reduces in size as the cloud collapses and the star enters the final stages of stellar evolution. The stellar wind is unable to support the wind-blown bubble against the surrounding gravitational collapse of the cloud.

In the more massive star cases, the stellar wind has a significant effect on the molecular cloud, carving channels and gaps through the cloud that are reminiscent of the interaction seen in our previous work (Rogers & Pittard 2013, 2014). Each star's wind halts the gravitational collapse of the cloud. The density, temperature, pressure and velocity of material in the cloud environment all span many orders of magnitude. The hottest gas typically occurs at the reverse shock of the stellar wind, and cools as it expands away from the cloud and mixes in with denser surrounding material. A multitude of weaker shocks form around the remaining dense clumps within the cloud and material is ablated from these into the stellar wind flow, as they also rearrange and form radially aligned spokes in the cloud. This change of structure allows self-shielding to occur and for cold molecular cloud material to survive for the lifetime of the star, both in these shielded spokes and entrained into the wind escaping the cloud along the channels.

In the most massive (120 M$_\odot$) star case, nearly half the molecular cloud is dispersed and destroyed during the final stages of stellar evolution, before the SN occurs. The channels through the wind bubble allow the forward shock of the SN to leave the wind structure very quickly through these 'leaky gaps'. In the cases of both the 60 and 120 M$_\odot$ stars, along these wind-carved channels, the forward shock leaves the computational volume after only 15 000 yr, at an average speed of over 4500 km s^{-1}, efficiently transporting kinetic and thermal energy into surroundings beyond the parent molecular cloud. The SN subsequently continues this dispersal and destruction, overrunning the structures formed during the wind phase. In all three cases, by 2.5 Myr after the SN, material with the characteristics of the warm neutral medium surrounds a low-density inner cavity (the central region of the SNR) at the original location of the isolated star.

It can be concluded from this work that stellar winds from the lower mass end of the range of stars undergoing core collapse have little effect on their parent cloud. In such cases, the cloud is likely to evolve subject to gravity, radiation pressure and external influences, until the star explodes. In contrast, higher mass stars are able to disperse and destroy the cold molecular material of the parent cloud even before SNe occur. Massive stars of intermediate mass carve channels and gaps through their parent clouds, allowing SN material to remain fairly hot and energetic as it escapes (see also Rogers & Pittard 2013, 2014; Paper II).

In this work, as in Paper II, we have taken a single initial condition, realistically formed from the action of the thermal instability, but none the less in isolation and at the lower end of molecular cloud masses. Molecular cloud masses in the Milky Way reach 10^{5-6} M$_\odot$, considerably more than the 16 500 M$_\odot$ of material in the cloud investigated here. The nature and distribution of this material is key to how the stellar winds and SN affect the molecular cloud. In future work, we will examine feedback into higher mass clouds and also account for radiative feedback effects.

REFERENCES

Agertz O., Kravtsov A. V., Leitner S., Gnedin N. Y., 2013, ApJ, 770, 25
Childs H. et al., 2012, in Bethel W., Childs H., Hansen C., eds, High Performance Visualisation – Enabling Extreme-Scale Scientific Insight. Chapman and Hall/CRC Press, Boca Raton, FL, p. 357
Dale J. E., Ercolano B., Bonnell I. A., 2012, MNRAS, 424, 377

Dale J. E., Ercolano B., Bonnell I. A., 2015, MNRAS, 451, 987
Dobbs C. L., Burkert A., Pringle J. E., 2011, MNRAS, 417, 1318
Ekström S. et al., 2012, A&A, 537, A146
Falle S. A. E. G., 1991, MNRAS, 250, 581
Field G. B., 1965, ApJ, 142, 531
Fierlinger K. M., Burkert A., Ntormousi E., Fierlinger P., Schartmann M., Ballone A., Krause M. G. H., Diehl R., 2016, MNRAS, 456, 710
Fogarty E., Frank A., Heitsch F., Carroll-Nellenback J., Haig C., Adams M., 2016, MNRAS, 460, 2110
Freyer T., Hensler G., Yorke H. W., 2003, ApJ, 594, 888
Freyer T., Hensler G., Yorke H. W., 2006, ApJ, 638, 262
Gatto A. et al., 2015, MNRAS, 449, 1057
Geen S., Hennebelle P., Tremblin P., Rosdahl J., 2016, MNRAS, 463, 3129
Girichidis P. et al., 2016, MNRAS, 456, 3432
Godunov S. K., 1959, Mat. Sb., 47, 271
Güdel M., Briggs K. R., Montmerle T., Audard M., Rebull L., Skinner S. L., 2008, Science, 319, 309
Harper-Clark E., Murray N., 2009, ApJ, 693, 1696
Koenig X. P., Leisawitz D. T., Benford D. J., Rebull L. M., Padgett D. L., Assef R. J., 2012, ApJ, 744, 130
Körtgen B., 2015, PhD thesis, Fachbereich Physik der Universität Hamburg, Hamburg
Körtgen B., Seifried D., Banerjee R., Vázquez-Semadeni E., Zamora-Avilés M., 2016, MNRAS, 459, 3460
Kurganov A., Tadmor E., 2000, J. Comput. Phys., 160, 241
Lopez L. A., Krumholz M. R., Bolatto A. D., Prochaska J. X., Ramirez-Ruiz E., 2011, ApJ, 731, 91
Lopez L. A., Krumholz M. R., Bolatto A. D., Prochaska J. X., Ramirez-Ruiz E., Castro D., 2014, ApJ, 795, 121
Mackey J., Haworth T. J., Gvaramadze V. V., Mohamed S., Langer N., Harries T. J., 2016, A&A, 586, A114
Martins F., Pomarés M., De Harveng L., Zavagno A., Bouret J. C., 2010, A&A, 510, A32
Ochsendorf B. B., Verdolini S., Cox N. L. J., Berné O., Kaper L., Tielens A. G. G. M., 2014, A&A, 566, A75

Offner S. S. R., Arce H. G., 2015, ApJ, 811, 146
Parker E. N., 1953, ApJ, 117, 431
Pellegrini E. W., Baldwin J. A., Ferland G. J., 2011, ApJ, 738, 34
Portegies Zwart S. F., McMillan S. L. W., Gieles M., 2010, ARA&A, 48, 431
Rogers H., Pittard J. M., 2013, MNRAS, 431, 1337
Rogers H., Pittard J. M., 2014, MNRAS, 441, 964
Rosen A. L., Lopez L. A., Krumholz M. R., Ramirez-Ruiz E., 2014, MNRAS, 442, 2701
Simpson C. M., Pakmor R., Marinacci F., Pfrommer C., Springel V., Glover S. C. O., Clark P. C., Smith R. J., 2016, ApJ, 827, L29
Townsley L. K., Feigelson E. D., Montmerle T., Broos P. S., Chu Y.-H., Garmire G. P., 2003, ApJ, 593, 874
Townsley L. K., Broos P. S., Garmire G. P., Bouwman J., Povich M. S., Feigelson E. D., Getman K. V., Kuhn M. A., 2014, ApJS, 213, 1
Van Loo S., Butler M. J., Tan J. C., 2013, ApJ, 764, 36
Van Loo S., Tan J. C., Falle S. A. E. G., 2015, ApJ, 800, L11
Vázquez-Semadini E., González R. F., Ballesteros-Paredes J., Gazol A., Kim J., 2008, MNRAS, 390, 769
Veilleux S., Cecil G., Bland-Hawthorn J., 2005, ARA&A, 43, 769
Vink J., de Koter A., Lamers H. J. G. L. M., 2000, A&A, 362, 295
Vink J., de Koter A., Lamers H. J. G. L. M., 2001, A&A, 369, 574
Walch S. K., Naab T., 2015, MNRAS, 451, 2757
Walch S. K., Whitworth A. P., Bisbas T., Wünsch R., Hubber D., 2012, MNRAS, 427, 625
Walch S. K. et al., 2015, MNRAS, 454, 238
Wareing C. J., Zijlstra A. A., O'Brien T. J., 2007, MNRAS, 382, 1233
Wareing C. J., Pittard J. M., Falle S. A. E. G., Van Loo S., 2016, MNRAS, 459, 1803 (Paper I)
Wareing C. J., Pittard J. M., Falle S. A. E. G., 2017, MNRAS, 465, 2757 (Paper II)
Winston E., Wolk S. J., Bourke T. L., Megeath S. T., Gutermuth R., Spitzbart B., 2012, ApJ, 744, 126

This paper has been typeset from a TEX/LATEX file prepared by the author.